

ROCKET BORNE MEASUREMENTS OF A NEAR-INFRARED VEHICLE  
INDUCED EMISSION WITH A NEWLY DESIGNED SPECTROGRAPH

By

Damon Burke

A Thesis Submitted to the  
Physical Sciences Department  
In Partial Fulfillment of the Requirements for the Degree of  
Master of Science in Space Science

Embry-Riddle Aeronautical University  
Daytona Beach, Florida  
Spring 2005

Copyright by Damon Burke 2005  
All Rights Reserved

**ROCKET BORNE MEASUREMENTS OF A NEAR-INFRARED  
VEHICLE INDUCED EMISSION WITH A NEWLY DESIGNED  
SPECTROGRAPH**

by

Damon Burke

This thesis was prepared under the direction of the candidate's thesis committee chair, Dr. Peter Erdman, Department of Physical Sciences, and has been approved by the members of his thesis committee. It was submitted to the Department of Physical Sciences and was accepted in partial fulfillment of the requirements for the Degree of  
Master of Science in Space Science

THESIS COMMITTEE:

\_\_\_\_\_  
Dr. Peter Erdman, Chair

\_\_\_\_\_  
Dr. John Olivero, Member

\_\_\_\_\_  
Dr. John Watret, Associate Chancellor

\_\_\_\_\_  
Dr. Gulamabas Sivjee, Member

\_\_\_\_\_  
Dr. Irfan Azeem, Member

\_\_\_\_\_  
Dr. James Wanliss, Member

\_\_\_\_\_  
MSSPS Graduate Program Coordinator

\_\_\_\_\_  
Department Chair, Physical Sciences

\_\_\_\_\_  
Date

## TABLE OF CONTENTS

ACKNOWLEDGEMENTS.....	V
ABSTRACT.....	VI
LIST OF FIGURES .....	VII
I. INTRODUCTION .....	1
II. INSTRUMENT.....	4
A. Introduction.....	4
B. Wavelengths.....	5
C. Optics.....	8
D. Cooling.....	12
E. Electrical .....	14
F. Baffle.....	17
III. EXPERIMENT .....	20
A. Assembly.....	20
B. Pre-Flight Testing .....	23
C. Flight.....	24
IV. DATA REDUCTION .....	28
V. RESULTS .....	35
A. Airglows.....	35
B. Door Heating.....	48
VI. CONCLUSIONS.....	50
REFERENCES .....	52
APPENDIX A.....	54
APPENDIX B.....	59

## ACKNOWLEDGEMENTS

The author wishes to express special thanks to the Thesis Chair, Dr. Peter Erdman, whose experience, expertise, and beneficial suggestions were crucial to the successful completion of this thesis. Appreciation is also extended to Dr. Patrick Espy, Professor Charles Bishop, and the Thesis Committee Members for their contributions and assistance.

An acknowledgement would be incomplete without a formal expression of gratitude towards the author's friends and family for the encouragement needed to complete the task.

One final sincere expression of appreciation goes to Amy Davenport for whom without such encouragement this thesis may have never been written.

## ABSTRACT

Author: Damon Burke  
Title: Rocket Borne Measurements of a Near-Infrared Vehicle Induced Emission with a Newly Designed Spectrograph  
Institution: Embry-Riddle Aeronautical University  
Degree: Master of Science in Space Science  
Year: 2005

In order to broaden current knowledge of a particular vehicle induced atmospheric glow, a modified Ebert-Fastie Spectrograph was designed and built at Embry-Riddle Aeronautical University for rocket borne observations of this glow. This instrument became a piggy-back payload on the Terrier-Orion SAMPLER 41.025 rocket payload launched from White Sands Missile Range in July, 2003. A photodiode detector array measured the mesospheric hydroxyl airglow emissions during the initial ascent as well as the vehicle induced glow through the mesopause at eight discreet bandpasses. Data collected shows moderate agreement with previous measurements by Murtagh et al. [1997] and López-Moreno et al. [1985] over similar wavelengths. With this data we attempt to show some correlations between the hydroxyl airglow and the vehicle induced glow.

## LIST OF FIGURES

Figure 1. Optical layout of instrument.....	6
Figure 2. BEAM4 trace of light path through instrument.....	9
Figure 3. Typical responsivity of InGaAs detectors .....	10
Figure 4. Drawing of optical arrangement at exit slit .....	11
Figure 5. External CAD view of payload with heat exchangers attached .....	13
Figure 6. Electrical schematic of data acquisition system .....	16
Figure 7. CAD drawing of inner baffle built with Pro/ENGINEER.....	18
Figure 8. Inner baffle prior to application of Ebanol C .....	18
Figure 9. Inner baffle after application of Ebanol C .....	19
Figure 10. CAD model of instrument built with Pro/ENGINEER .....	21
Figure 12. Instrument loaded into payload section prior to final assembly.....	25
Figure 13. Payload being purged with nitrogen on launch rail prior to lift-off .....	26
Figure 14. Vehicle velocity.....	27
Figure 15. Spectrogram of Y axis magnetometer data showing a constant spin rate until apogee (around 200 seconds).....	29
Figure 16. Drifting electrical noise evident in 1.364 $\mu\text{m}$ center wavelength detector.....	31
Figure 17. Vehicle spin evident in recombined optical data.....	32
Figure 18. Effect of selected bandpass filter on overall flight data .....	33
Figure 19. Data measured from 1.609 $\mu\text{m}$ center wavelength detector .....	36
Figure 20. Volume emission rate of hydroxyl nightglow .....	37
Figure 21. Vehicle induced glow compared to atomic oxygen model .....	39
Figure 22. Vehicle glow from six detectors normalized to the vertically integrated hydroxyl emission brightness .....	40

Figure 23. Relative integrated airglow intensities of various hydroxyl transitions in the near-infrared with a full-width half maximum 0.05 $\mu\text{m}$ triangular bandpass.....	41
Figure 24. Relative contributions to detector input from various OH transitions .....	42
Figure 25. Ratio of vehicle induced glow at 101 km to integrated airglow seen from lower altitudes. ....	43
Figure 26. Integrated brightness from López-Moreno et al. publication [1985] .....	45
Figure 27. Integrated brightness of three detectors similar to those targeted by López-Moreno et al. [1985] .....	46
Figure 28. Derived atomic oxygen density compared with measurements from Murtagh et al. [1997] .....	47
Figure 29. Data presented in the Murtagh et al. [1997] publication .....	48
Figure 30. Heating of instrument door during ascent .....	49

## I. Introduction

In situ atmospheric measurements provide a key source for understanding composition and behavior of the upper atmosphere. However, any instrument or vehicle used to take measurements has a potential for introducing contaminants into the measurement. Oils, dirt, and gases from handling the instrument before flight can become airborne during flight and introduce artifacts into the atmosphere. While care can be taken to eliminate any known contaminants from acquired data, the actual flight vehicle itself can alter the dynamics of the environment of interest.

Vehicle induced radiation is a well documented problem almost as old as sounding rocket research itself. While many of these glows have been attributed to exhaust gases influencing local chemistry, a few glows, found by forward-looking instruments, have shown a connection to atomic oxygen density [Clemesha et al., 1987; Clemesha et al., 1988; Conway and Meier, 1987; Swenson et al., 1985; Yee et al., 1985; Yee and Abreu, 1983]. López-Moreno et al. [1985] discovered a vehicle induced emission they referred to as a “contaminating glow” in three of their four photometers with center wavelengths of 1.55  $\mu\text{m}$ , 1.65  $\mu\text{m}$ , and 1.70  $\mu\text{m}$ . The fourth photometer at 1.27  $\mu\text{m}$  failed to detect a similar glow. They believed that hydrocarbons attached to the vehicle surface interacted with atomic oxygen to generate excited hydroxyls. Murtagh et al. [1997] discovered a similar glow with a 1.53  $\mu\text{m}$  photometer while an identical photometer at 1.27  $\mu\text{m}$  detected no such contamination. In this case, simultaneous

atomic oxygen measurements taken by Murtagh et al. showed that the contaminating radiation was proportional to the atomic oxygen density.

Both López-Moreno et al. and Murtagh et al. used photometers with narrow bandpass filters to detect the radiation, creating significant gaps in the spectrum. Murtagh measured wavelength regions similar to those measured by López-Moreno, thus failed to provide additional spectral data to help deduce a mechanism for this radiation.

Since the transitional area of the atmosphere between 70 km and 130 km is of particular interest to atmospheric physicists, further investigation of this glow is warranted. Future research projects taking near-infrared measurements in the mesopause are likely to encounter similar contamination from this vehicle induced emission. Knowing the mechanism causing the glow could provide physicists the opportunity of designing their instrument to acquire the necessary data while avoiding the contamination.

A proper analysis of this glow should start with a broad spectrum including previously measured wavelengths. In addition, good altitude resolution and an effective signal to noise ratio (SNR) are necessary to compare with previous flights. Previous measurements showed a hydroxyl airglow around 20 kiloRayleigh and a vehicle induced emission as strong as 60 kiloRayleigh. A simultaneous measurement of the hydroxyl airglow region during the same flight would be useful since both authors believed hydroxyl radicals were responsible for the resulting glow.

Presented here is an instrument designed to gather this information, as well as the data acquired from its first launch. This specially designed dispersive near-infrared spectrograph was launched as part of the SAMPLER payload 41.025 aboard a Terrier

MK-12 Improved Orion rocket at 1:02 AM local time on July 15<sup>th</sup>, 2003 from White Sands Missile Range in New Mexico (32.23N, 106.29W). It included a series of eight cooled InGaAs detectors with 50 nm FWHM bandpass. The instrument looked forward 30° off the vehicle thrust axis and measured emissions between 1  $\mu\text{m}$  and 1.63  $\mu\text{m}$  to an apogee of 127 km.

The data acquired shows good agreement with previous measurements. A strong airglow was measured through the hydroxyl airglow layer [Meinel, 1950] and the vehicle induced glow was noticeable in all detectors. We provide an analysis of the acquired data and provide some theories into the active mechanism behind the vehicle induced glow.

## II. Instrument

### A. Introduction

The traditional Ebert-Fastie Monochromator has been used extensively in rocket borne measurements for decades. In 1889, Hermann Ebert published his design for a new type of monochromator based on the Czerny-Turner spectrometer. Fastie modified this design by applying curved entrance and exit slits to reduce astigmatism and adding some rudimentary baffles to prevent scattered light from entering the detectors directly [Fastie, 1952]. Fastie followed up on his initial design by shortening the instrument and extending it into the infrared region. The choice of curved slits eliminated wavelength overlapping introduced from the use of a plane grating and a spherical mirror [Fastie, 1952].

Fastie applied a motor to the grating shaft of his monochromator allowing it to scan a series of wavelengths. A scanning spectrometer allows for scans over a wavelength region to be made with only a single detector at the expense of an extended scanning period [Fastie, 1952]. This robust and stable design resulted in an ideal instrument for sounding rocket measurements.

We followed the general Ebert-Fastie design when building our instrument. Incoming light is limited by an entrance baffle to reduce entrance angles. A bandpass filter was added to limit allowed wavelengths so scattered and diffracted light at other wavelengths wouldn't be included in our data. Light coming through the entrance slit is reflected off an internal spherical mirror onto a diffraction grating. The grating reflects

and diffracts light at different angles based on the wavelength allowing specific wavelengths of light to be selected by rotating the grating. The dispersed light is reflected off the spherical mirror again to focus the light into the exit slit (see figure 1).

To simplify the data acquisition system, we used a simplified version of the spectrometer known as a spectrograph. A spectrograph uses multiple detectors across the focal plane rather than scanning across a single detector. The standard Ebert-Fastie monochromator has a limited focal plane for exit slits. In order to use multiple detectors a modified version of this monochromator flown on the Bow Shock Ultraviolet Payload was used as a basis for this design [Erdman et al., 1993]. The grating was shifted farther from the entrance slit allowing multiple exit slits to be used with a single set of optical elements.

## B. Wavelengths

Murtagh et al. [1997] determined that “no contamination was detectable ... by broadband uv/visible photodiode photometers.” This provides some indication that the contaminating emission is due to population changes in vibrational states of excited molecules. Thus an instrument designed for a broad examination of the near-infrared region would provide the most useful information.

In designing this instrument two wavelengths of particular interest included  $\sim 1.54$   $\mu\text{m}$  and  $1.27$   $\mu\text{m}$  since they were both measured on previous flights. In addition, measurements of wavelengths shorter than  $1.27$   $\mu\text{m}$  would indicate whether the energy cut-off for the radiation was longer than  $1.27$   $\mu\text{m}$  or if  $1.27$   $\mu\text{m}$  was simply not a preferential emission for this mechanism.

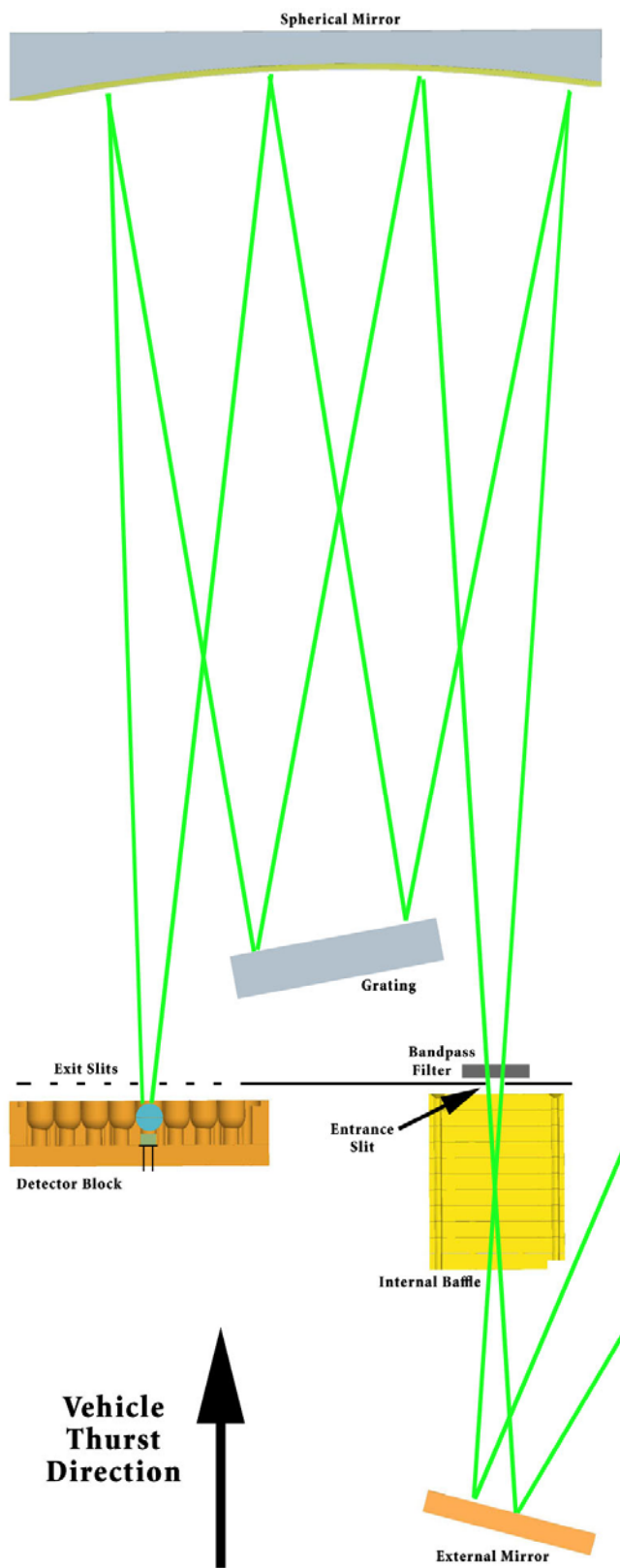


Figure 1. Optical layout of instrument.

One consideration is whether the vehicle induced glow can be attributed to a particular upper energy state of OH or a particular  $\Delta v$  transition. Murtagh et al. [1997] measured a strong vehicle emission at 1.53  $\mu\text{m}$ . This wavelength would be dominated by emissions generated by OH (3,1) and OH (4,2) transitions.

Synthetic hydroxyl emission spectra [P. Espy, *private communication*] generated from the Mies transition probabilities [Mies, 1974] demonstrate that an OH (4, 2) transition would radiate just long of 1.6  $\mu\text{m}$ . To determine if the fourth vibrational energy level of OH is preferentially populated an investigation of the OH (4,1) transition which emits between 1  $\mu\text{m}$  and 1.07  $\mu\text{m}$  is warranted.

Another OH transition of interest is the OH (8,4) transition which radiates at wavelengths just short of one micron. The higher energy states were considered a non-critical measurement for this flight. Since neither previous measurement found contaminating radiation at 1.27  $\mu\text{m}$ , with OH (7,4) and OH (8,5) emitting heavily at that wavelength, we wouldn't expect significant radiation from the upper level states of OH. This yields a preferred measurement range from 1  $\mu\text{m}$  to just long of 1.6  $\mu\text{m}$  for measuring OH radiation.

To provide measurements similar to previous flights, we attempted to closely match the flight conditions of Murtagh et al. The instrument looked forward, thirty degrees off of the vehicle thrust axis, through an opening in the skin. Since the instrument is looking forward it should reveal any existing glow above it as a constant brightness which appears to decrease as the vehicle passes through the layer. Any increase in signal with altitude is probably generated due to vehicle interactions with the atmosphere.

### C. Optics

Due to cost and time constraints, we used a 300 mm focal length first surface mirror made by Hyperfine, Inc. The mirror was an aluminum surface giving moderate reflection in the visible and near infrared. The mirror substrate was made of Zerodur Schott glass for minimal thermal expansion. Zerodur has a typical coefficient of thermal expansion of  $5\text{E-}8\text{ K}^{-1}$  which is less than one tenth the expansion of Pyrex. Since the instrument would be cooled after calibration it was important to minimize thermal contraction of the mirror.

Using photodiodes in TO-18 cans allowed for a center to center spacing of 8 mm between detectors. Eight detectors were placed in a line bringing the furthest detector 136 mm from the entrance slit. A pair of focusing lenses were used to focus the light passing through the entrance slit onto the detector. As detectors are placed farther from the entrance slit the light entering the focusing lenses diverges farther from the optical axis. For small distances the optics can be shifted slightly off-axis with the detector to compensate for the change in incoming light angle. Ray traces showed that detectors beyond 136 mm from the entrance slit would require significant shifting of optical elements and a greater loss of light due to steep entrance angles.

A 5mm square aperture was chosen for the entrance and exit slits. This width allowed for a moderate amount of light to enter the system while not being long enough to require curvature in the slit shape. This configuration provides a triangular bandpass with a full-width half maximum of  $0.05\ \mu\text{m}$ . Numerous ray traces were performed with Stellar Software's BEAM4 software to determine the optimal instrument configuration (see figure 2). A plane grating with 300 grooves / mm blazed at  $1\ \mu\text{m}$  (first order) with

60+% groove efficiency was selected. This grating provided a range of first order diffracted wavelengths between 1  $\mu\text{m}$  and 1.61  $\mu\text{m}$  in the focal plane across a 56 mm distance.

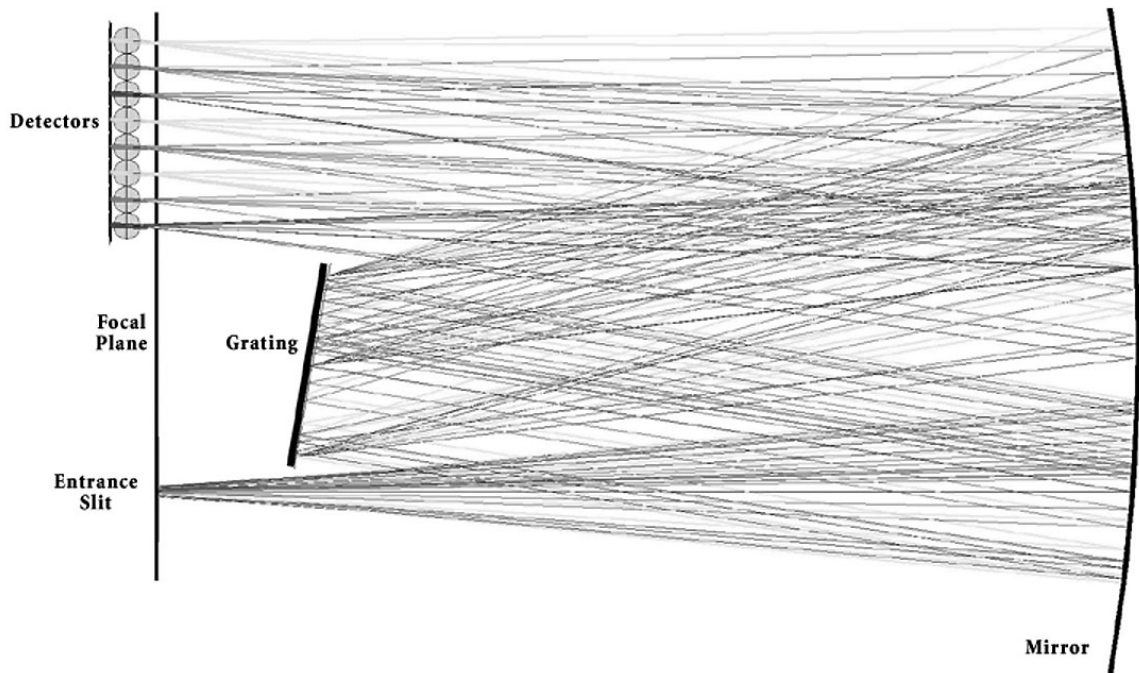


Figure 2. BEAM4 trace of light path through instrument.

The grating was set to a fixed angle of 9.96 degrees with respect to the focal plane. This achieved the goal of selecting the 1.53  $\mu\text{m}$  center wavelength on the second to last detector. The center wavelengths for each detector were 1.029  $\mu\text{m}$ , 1.113  $\mu\text{m}$ , 1.197  $\mu\text{m}$ , 1.281  $\mu\text{m}$ , 1.364  $\mu\text{m}$ , 1.446  $\mu\text{m}$ , 1.530  $\mu\text{m}$ , and 1.609  $\mu\text{m}$ . These wavelengths cover the range from 1  $\mu\text{m}$  to 1.61  $\mu\text{m}$  while still staying fairly close to the target wavelengths of  $\sim$ 1.54  $\mu\text{m}$ , 1.27  $\mu\text{m}$ , and 1.65  $\mu\text{m}$ .

Fermionics' Indium Gallium Arsenide (InGaAs) photodiode detectors were used. Standard InGaAs detectors have a strong responsivity between .950  $\mu\text{m}$  and 1.65  $\mu\text{m}$ , covering the full range of the instrument. Low capacitance and low dark current make these detectors well suited for this experiment. Responsivity drops two orders of magnitude between 1.65  $\mu\text{m}$  and 1.75  $\mu\text{m}$  to help minimize longwave blackbody contamination (see figure 3). High linearity, with respect to both signal level and temperature, simplify data reduction.

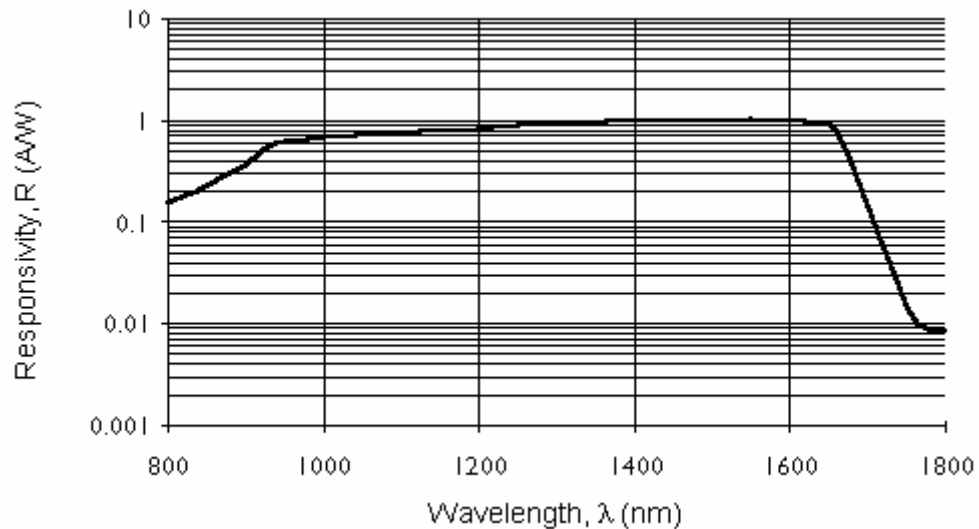


Figure 3. Typical responsivity of InGaAs detectors (from Fermionics website).

To help maintain thermal stability throughout the flight the detectors were thermally sunk to a piece of 76.2 mm x 76.2 mm x 19.05 mm copper-beryllium chosen for its high thermal capacity and ease of machining. The detectors and associated focusing lenses were recessed into the copper-beryllium block and the block was mounted to the focal plane of the instrument (see figure 4).

Second order diffractions off the grating would direct visible light onto the detectors. Since these detectors are sensitive to visible light a Spectrogon long wavepass filter P-E Lambda 9-1 was placed at the entrance slit. This 25.4 mm diameter glass substrate filter blocked almost all light short of 0.9  $\mu\text{m}$  and kept dust and dirt from entering the instrument through the entrance slit.

InGaAs detectors with a detector area of 1  $\text{mm}^2$  were chosen to minimize noise inherent in larger detector areas. To focus the light from the 5 mm x 5 mm exit slit down onto the 1 mm x 1 mm square detector area a series of optical ray traces were performed with various combinations of stock lenses from Edmund Scientific. Stellar Software's BEAM4 was used to iteratively modify detector placement as well as optical lens placement and orientation to determine the greatest throughput. A split spherical ball lens design was determined to provide the best throughput.

Two hemispherical 8 mm diameter lenses were separated by a 0.05 mm thick Teflon washer. These were placed inside a hole in the copper and held against the copper with a Teflon tube. The tube cradled the lens at one end and was pressed in place by a brass sheet at the other end providing a firm hold on the lenses while allowing absorption of vehicle induced vibrations and shocks (see figure 4).

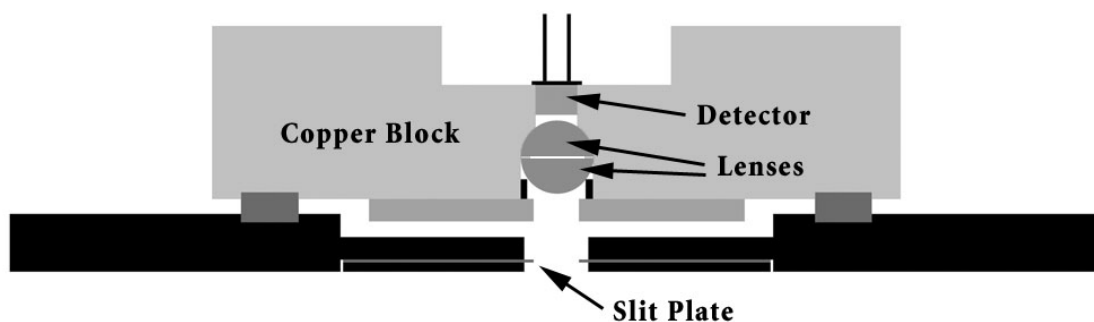


Figure 4. Drawing of optical arrangement at exit slit.

#### D. Cooling

Blackbody emissions around  $1.6 \mu\text{m}$  contribute a significant amount of light at  $20^\circ\text{C}$ . Since the entire detector body could contribute blackbody emissions onto the detector it was necessary to cool the instrument. Preliminary SNR calculations were performed by undergraduates Joel Reese and Kavan Modi as a project for their Optics class. They determined that a temperature of  $-10^\circ\text{C}$  would provide a SNR of 100. A temperature of  $-20^\circ\text{C}$  was finally chosen as a safe launch temperature.

Heat exchangers were chosen as the optimal method of cooling the instrument for flight. They consisted of a copper tube press-fit into grooves machined into an aluminum plate. Good thermal conduction and a convenient mounting surface made these ideal for mounting to the side of the spectrograph. One heat exchanger was placed on each side of the instrument (see figure 5).

AD590 temperature transducers were placed throughout the instrument, cooling lines, and payload section so thermal properties could be monitored during flight. The Analog Devices AD590 provides a linear current output of  $1 \mu\text{A}/\text{K}$ . A  $10 \text{ k}\Omega$  resistor was placed across the output of the AD590. A volt meter placed across this resistor would read one volt per 100 K of temperature. A hand-held device was also constructed to give real-time preflight readout of all payload temperatures via an access panel in the side of the payload.

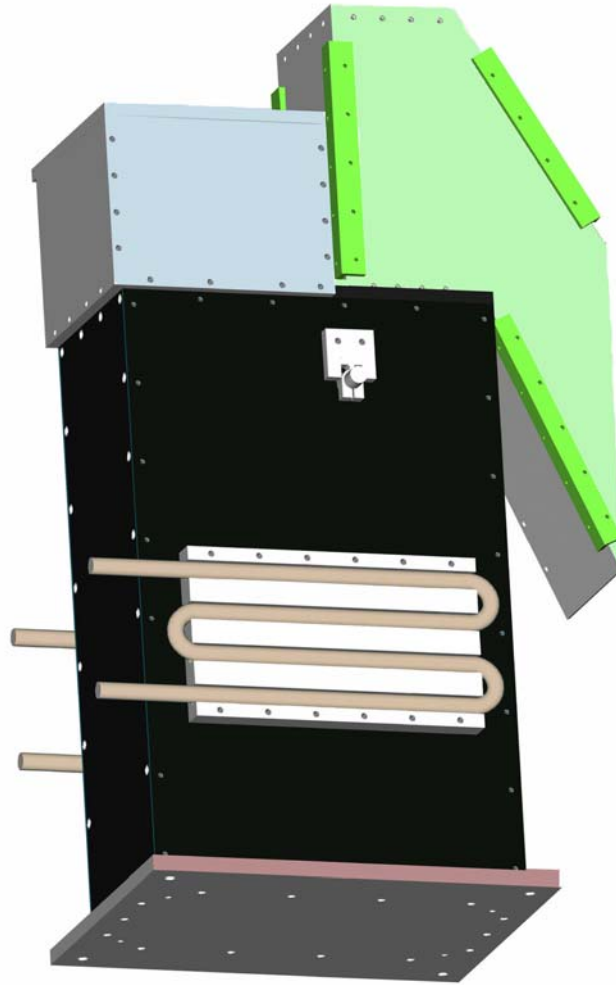


Figure 5. External CAD view of payload with heat exchangers attached.

Liquid nitrogen was chosen as a simple payload coolant. A standard Dewar of nitrogen has an inherent pressure building mechanism built in and is fairly inexpensive. No additional equipment was needed to push the nitrogen up the launch rail to the payload. Polypropylene 3/8" diameter tubing was selected to bring the liquid nitrogen from the Dewar to the payload prior to launch. Polypropylene remains fairly flexible at  $-196^{\circ}\text{C}$  yet doesn't suffer from the accidental kinking susceptibility of copper tubing. AP/Armaflex 25/50 insulating tubes from Armacell Engineered Foams provided a

convenient method of insulating the cooling lines along the launch rail. This tubing had a 3/8" inner diameter and 3/4" wall thickness and came in 8 foot lengths. By using individual segments we could easily add or remove tubing as the length of cooling line was extended or cut on site.

#### E. Electrical

The data acquisition system uses a dual input integrator and 20 bit analog to digital (A/D) converter chip called DDC112 made by Burr-Brown (now part of Texas Instruments). Designed specifically for low current applications, this chip allows the photodiode to be wired directly into the chip without an additional pre-amp. An external reference voltage charges internal capacitors before each integration. Capacitor charge is leaked through the photodiodes (proportionately to the incident light received at the detector) during a clocked integration period. The remaining voltage on the capacitor is digitized into a 20 bit word and clocked out of the chip along the serial line.

Each input on the DDC112 uses dual integrators and two capacitors allowing simultaneous integration of the current signal as well as digitization of the value from the previous integration period. This allows for continuous data acquisition at the expense of inequalities between capacitors and integrators generating different offsets in the data. This can all be handled in post-flight data analysis to keep distortions to a minimum.

The DDC112 requires a number of control lines. An external 10 Mhz clock is responsible for driving all DDC112 functions. A "convert" line toggles between high and low to direct which inverter is processing the incoming signal. Once the data is integrated it is clocked out via an external clock provided by the rocket telemetry system.

The data acquisition system for the spectrograph holds four DDC112 chips to handle the eight photodiodes. A crystal oscillator provides the 10 Mhz clock signal for the A/D chips. Since the telemetry system only provides a momentary “data enable” signal and the prerequisite “data clock” stream, a pair of flip-flops generate the additional required signals. A series of buffers are used to synchronize the enable, data clock, and convert lines with the 10 Mhz clock signal to help minimize noise. The reference voltage is provided by a high accuracy zener diode coupled with an op-amp to provide the current necessary to charge all the capacitors quickly.

To help reduce noise of the 10 Mhz signal coupling into the detector inputs, a four layer circuit board was custom designed in the Atmospheric Physics Research Lab at Embry-Riddle Aeronautical University (see figure 6). This board uses ground and power planes to minimize impedance of power to the chips as well as provide a shield around detector inputs. Inputs from the telemetry system were optically isolated to prevent any external electrical noise from being passed into the data acquisition system. Power to the circuit board is provided by a Datel DC-DC converter with isolated ground to help eliminate any electrical noise from the vehicle power system.

In flight, the detectors were sampled at 40 Hz driven by the telemetry enable signal. This sampling rate provided altitude resolution of 30 meters or better throughout the altitude of interest. Serial data was clocked out of the DDC112 chips at 40 kHz driven by the telemetry data clock signal. Initial experiments showed that varying the data clock rate had no effect on integrator noise.

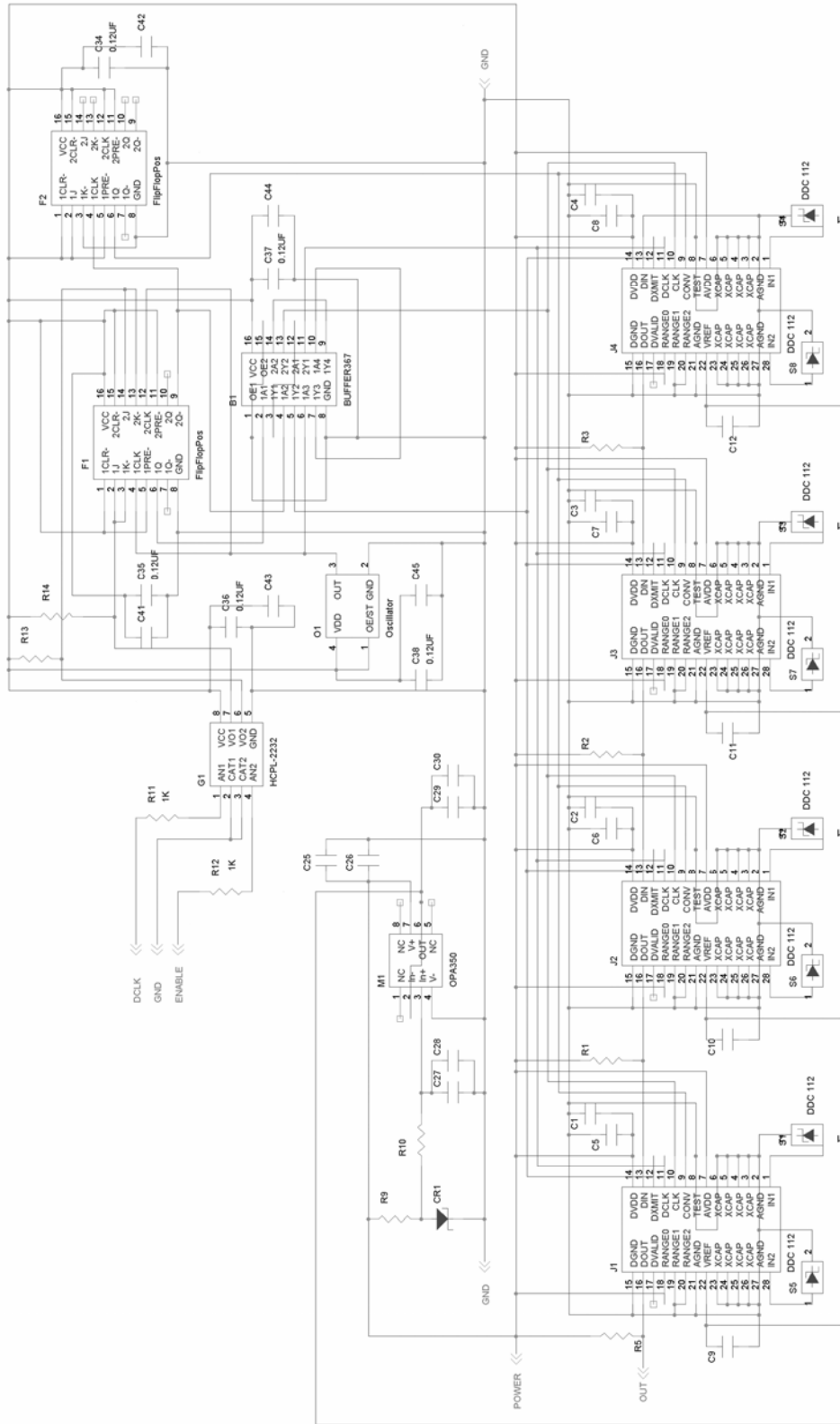


Figure 6. Electrical schematic of data acquisition system.

## F. Baffle

To prevent unwanted light from entering the instrument, a two phase optical baffle was developed. The outer baffle is intended to ensure that only glow from the atmosphere enters the optical system. Due to size limitations in the instrument area, a folded outer baffle was used. A single first surface mirror directs light along the instrument look direction down into the inner baffle. Flat black paint was applied to the insides of the outer baffle to decrease light scattering off internal surfaces. Since the instrument must look out of the vehicle skin, the baffle must ensure that any light scattered off the door's edges cannot pass into the instrument. Scattered earth-shine would provide enough light to saturate the detectors.

The inner baffle system was designed to limit the  $f/\#$  of the incoming light. The baffle consists of a stack of ten 0.176" thick copper rings with sheets of 0.005" thick phosphor-bronze sandwiched between the rings (see figure 7). The phosphor-bronze sheets have square holes cut in the center to allow light to pass through. The top sheet of phosphor-bronze has an 11.5 mm x 11.5 mm square hole cut as the limiting aperture of the system while the rest of the sheets have a 24.4 mm x 24.4 mm square hole.

The copper and phosphor-bronze materials were chosen to allow the application of an oxidizing agent known as Ebanol C from Enthone. Ebanol C attacks copper surfaces and creates a thick black coating with a highly textured finish that resembles felt. This coating was desired to significantly reduce the intensity of any scattered light (see figures 8 and 9).

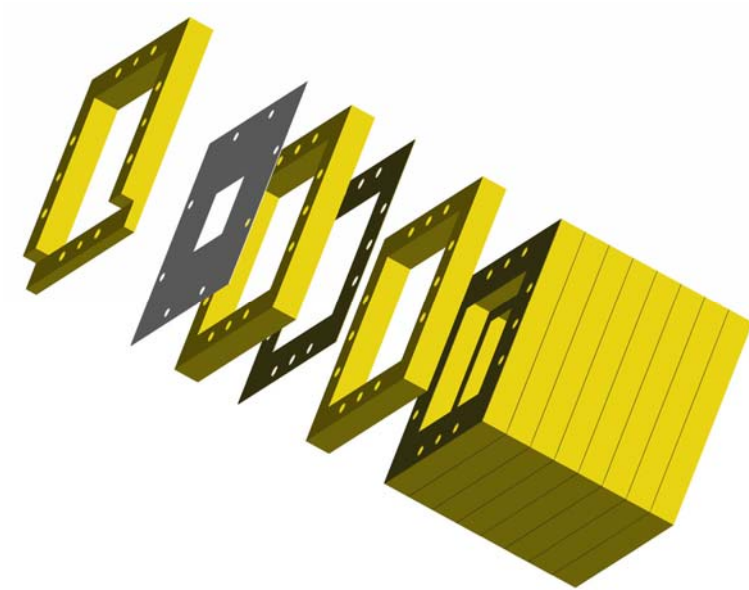


Figure 7. CAD drawing of inner baffle built with Pro/ENGINEER.

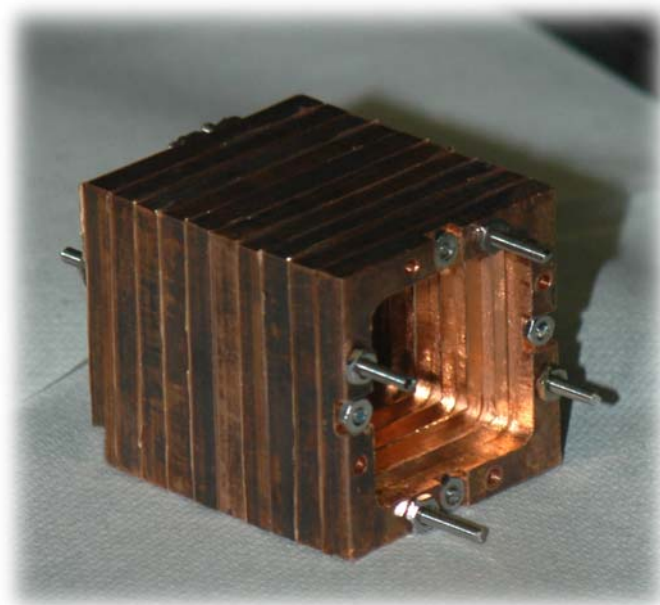


Figure 8. Inner baffle prior to application of Ebanol C.



Figure 9. Inner baffle after application of Ebanol C.

Stellar Software's BEAM4 and AutoCAD by Autodesk, Inc. were used to develop a baffle in which the multiple edges of the baffling system could not scatter light directly into the optical path. The 24.4 mm square holes were chosen because their placement and size could scatter light outside the  $f/6$  instrument path but such scattered light could not reach the spherical mirror without additional reflections.

### III. Experiment

#### A. Assembly

Since the payload temperature would vary 40°C between alignment and flight, it was necessary to build a robust structure to house the optical elements. The frame of the spectrograph was milled out of a single ingot of solid aluminum. The surfaces and holes securing the optical elements were machined directly into the frame to ensure proper alignment and spacing between them (see figure 10).

Optical alignment of the instrument was simplified by the use of the second order diffractions off the grating. By removing the black glass filter various emissions in the visible spectrum could be used. A mercury discharge lamp was placed at the entrance slit. The second order diffraction of the 0.546  $\mu\text{m}$  mercury line just begins to fill the second exit slit at proper alignment. The grating angle was tweaked and final optical alignment was performed with this particular emission as a guide.

Calibration of the spectrograph was performed inside a sealed chamber in the Atmospheric Physics Research Lab at Embry-Riddle Aeronautical University. Although the payload was designed to operate in a vacuum environment it was not necessary to calibrate the system in a vacuum. The chamber was purged with dry nitrogen gas prior to calibration to eliminate moisture due to water vapor's strong absorption bands between 1  $\mu\text{m}$  and 2  $\mu\text{m}$ . Liquid nitrogen was pushed through copper tubes submersed in warm water baths to maintain a constant temperature source of dry nitrogen.

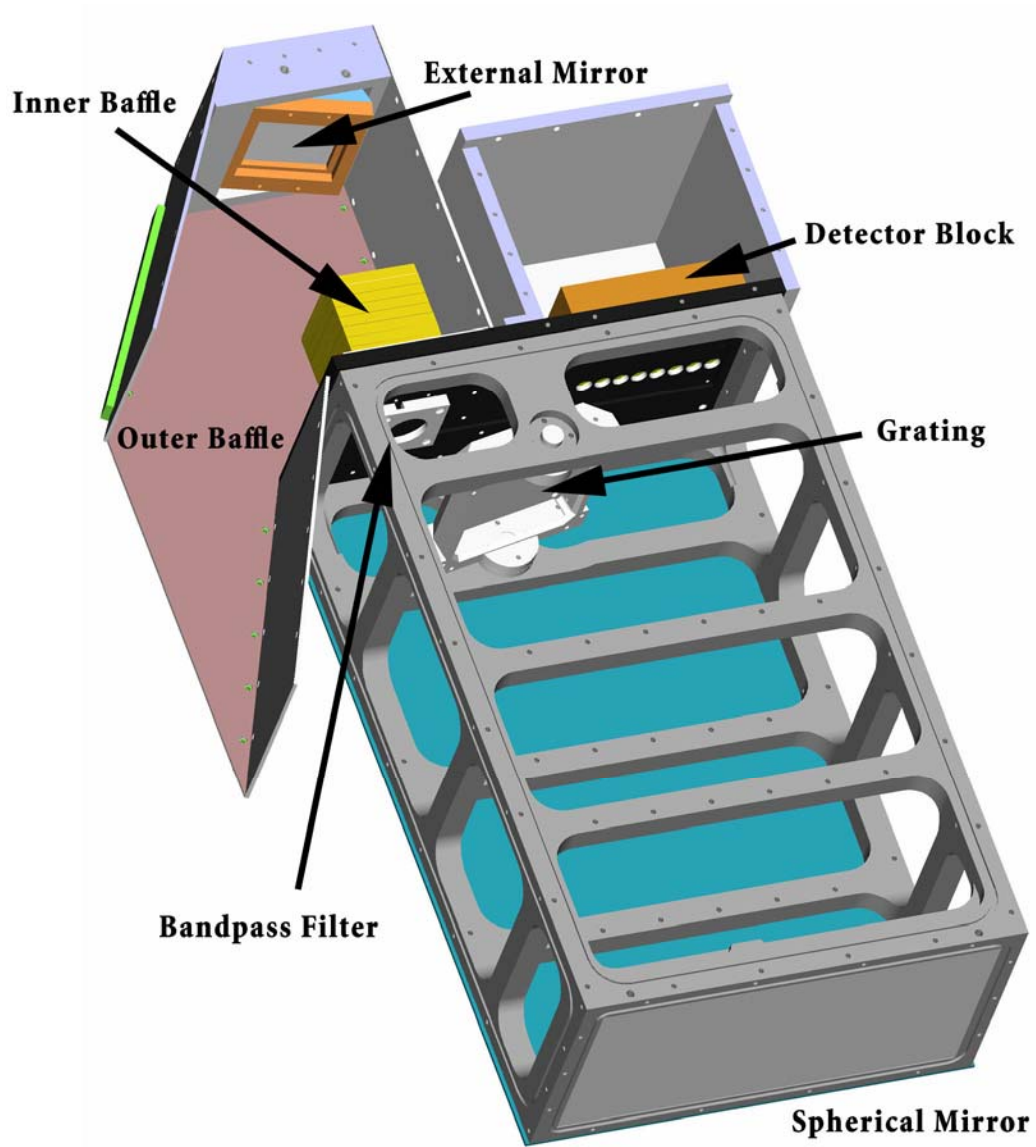


Figure 10. CAD model of instrument built with Pro/ENGINEER.

Labview Software by National Instruments was used to simulate the signals delivered to the instrument by the telemetry section during flight and to acquire signal output from the instrument. NI6602 and DIO-32HS data acquisition cards were used to deliver the signals to and from the computer.

Liquid nitrogen was pumped through the heat exchanger to bring the payload temperature down to the expected flight temperature of  $-20^{\circ}\text{C}$ . The AD590 temperature monitors installed for flight were used in conjunction with previously calibrated thermocouples to verify accuracy of the temperature monitors.

A calibrated high temperature CS1050-100 Cavity Blackbody from Electro Optical Industries, Inc. provided a uniform radiation source at  $1050^{\circ}\text{C}$ . This emission was directed onto a lambertian surface made up of powdered Halon. The instrument was pointed at the Halon screen and measurements were taken.

Instrument readings were taken regularly during the nitrogen purge to watch for variations due to atmospheric absorption. A humidity sensor was placed inside the chamber and compared with optical data. As relative humidity dropped below 10% the changes in instrument brightness fell below the noise floor of the detectors. All calibrations were performed below this humidity threshold.

The blackbody aperture was adjusted to verify linearity of the detectors with respect to incident brightness. Once all linearity checks were completed an absolute irradiance calculation was determined for each detector. A cooled metal plate was used to occult the blackbody path. With this occulting plate we could calculate “dark values” for the detectors. These readings accounted for integrator bias, dark current, shunt resistance, and capacitance variations in the system.

Dark values were subtracted from the brightness values measured when the screen was illuminated. This gave an absolute difference in signal based on a particular amount of incident light. Dividing the brightness by the full scale percentage gave a saturation brightness for each detector. This value became a scaling factor to convert flight data into absolute brightness.

## B. Pre-Flight Testing

The instrument frame, plates, and all metal within the optical path was washed with acetone and ultrasonically cleaned in Alconox cleaner before assembly. Optical assembly took place in a clean room to minimize contaminants.

Without any sophisticated modeling software we decided to test the payload cooling by experimentation. During preflight cooling the instrument section would be located about 50 feet off the ground on the launch rail. A summer launch from White Sands Missile Range could expose the payload and cooling lines to ambient temperatures of 40°C in the shade. To simulate this we placed the enclosed payload section on the roof of the Lehman Engineering and Technology Building at Embry-Riddle Aeronautical University's Daytona Beach campus. We chose a typical summer day in Florida with temperatures near 35°C and full sunlight.

The insulated polypropylene tubing was hung off the side of the building exposing it to direct sunlight. Temperature values in the payload were monitored while the liquid nitrogen Dewar was throttled open. Tests showed that this configuration provided sufficient cooling rates to keep the payload at the desired temperature in expected conditions.

### C. Flight

The instrument was located in a 17.25” diameter aluminum cylindrical skin approximately 22” long (see figure 12). Due to vehicle stability concerns the instrument section was placed aft of the telemetry section. The center of the instrument window was located approximately 74” behind the vehicle stagnation point. After nose-cone deployment (prior to instrument door deployment) the vehicle nose becomes a blunt flat surface across the diameter of the payload generating a wide shockwave.

In order to utilize the folding baffle design the instrument was mounted upside-down inside the payload skin. Half inch long stainless steel spacers were used to thermally isolate the instrument from the deck plate. Both deck plates were lined with quarter inch thick medium density Pyropel material from Albany International. This material provides excellent thermal insulation while allowing trapped gasses to easily escape. The skin surface was internally lined with a single layer of eighth inch thick low density Pyropel.

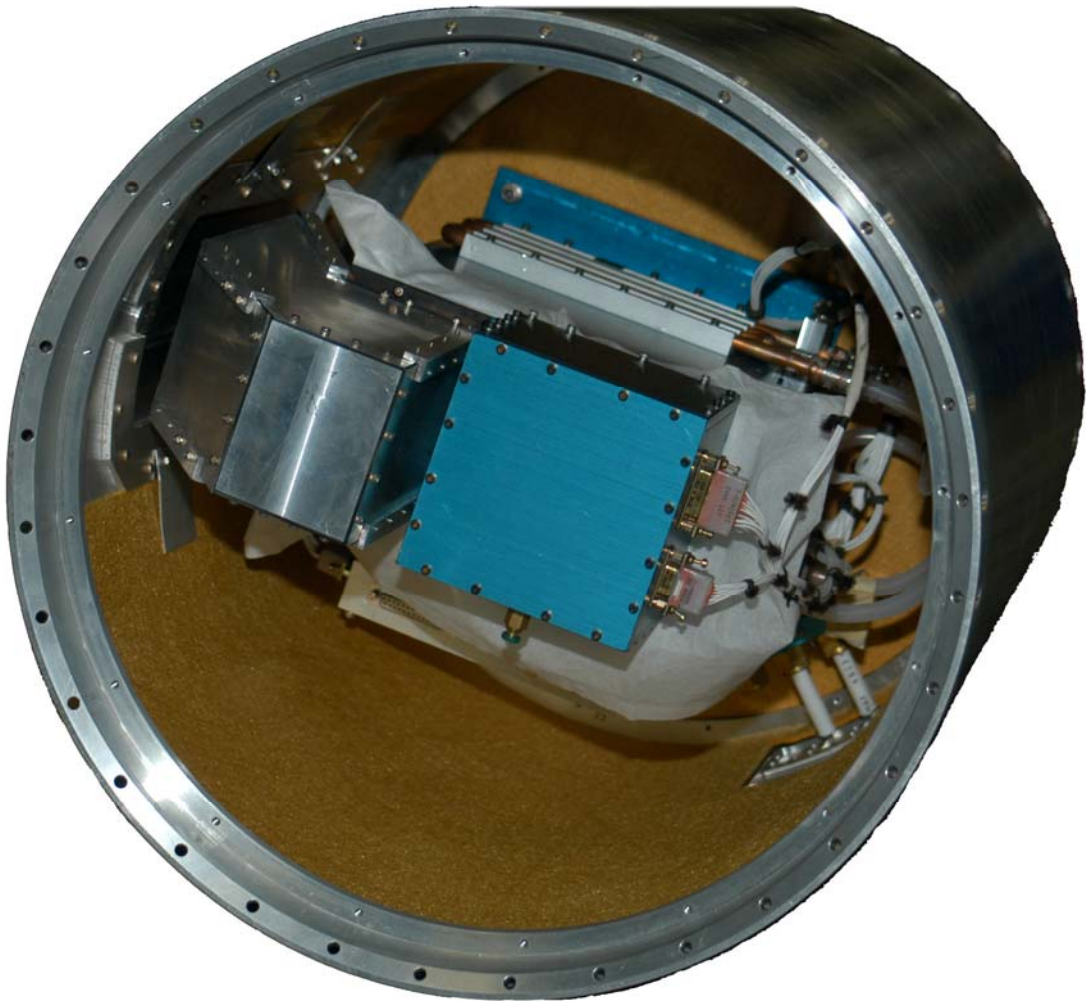


Figure 12. Instrument loaded into payload section prior to final assembly.

The instrument section was purged with dry nitrogen while on the launch rail for 24 hours prior to launch to help eliminate any potential condensation on the instrument (see figure 13). Three hours prior to launch the liquid nitrogen Dewars were opened and coolant pumped into the instrument. A temperature of  $-20^{\circ}\text{C}$  was stabilized after an hour of cooling and maintained until launch. Data acquisition began ten minutes prior to launch and maintained until loss of signal at touchdown.

The payload launched aboard a Terrier MK-12 Improved Orion at 1:02 AM local time on July 15<sup>th</sup>, 2003 from White Sands Missile Range in New Mexico. Data acquired by the spectrograph was transmitted in real time to the tracking station at White Sands Missile Range. The vehicle landed by parachute approximately fourteen minutes later and was recovered by helicopter shortly after dawn (five hours later). All payload components behaved as expected.

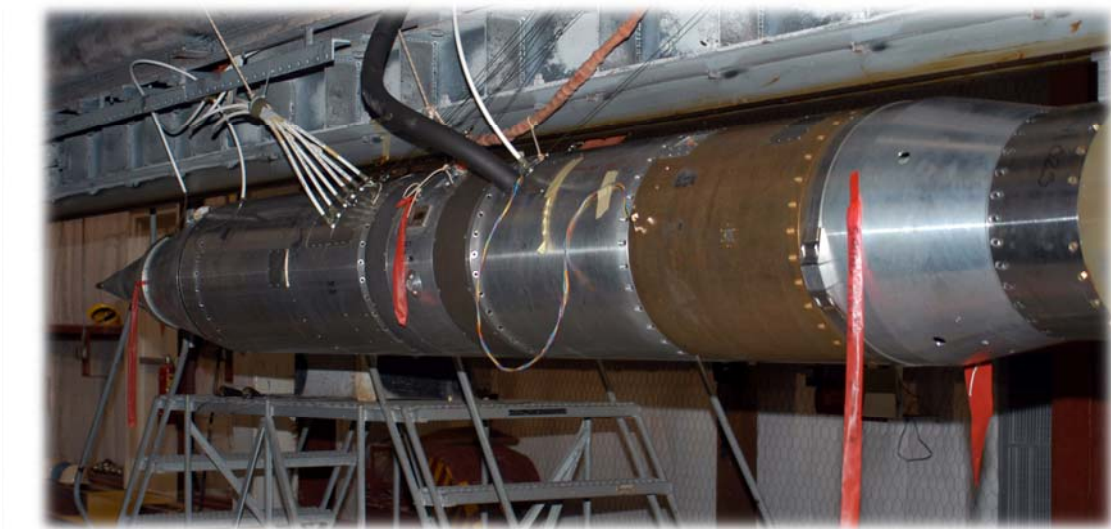


Figure 13. Payload being purged with nitrogen on launch rail prior to lift-off.

The total payload weight was 589 lbs. at launch and reached an altitude of 127.7 km (approximately one sigma higher than predictions). Velocity through the vehicle induced glow region remained below 800 m/s (see figure 14).

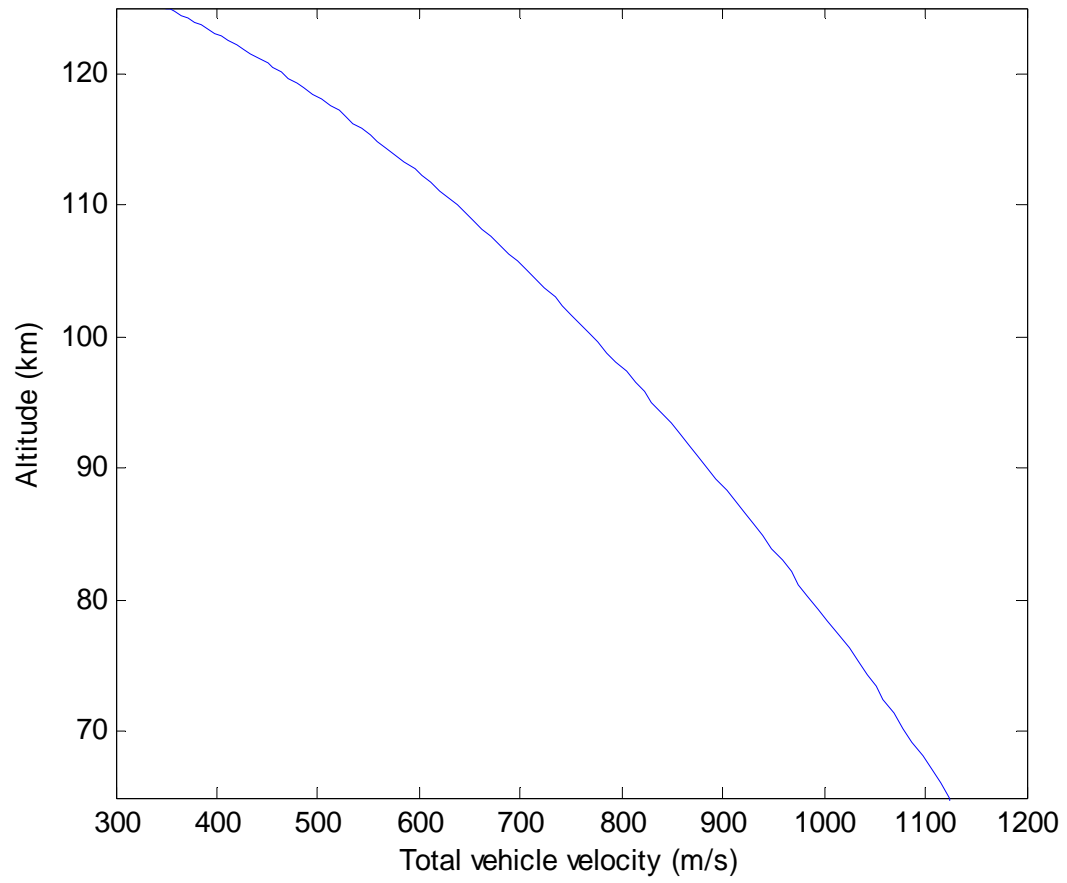


Figure 14. Vehicle velocity.

#### IV. Data Reduction

In-flight data was transmitted as a stream of 160 data bits consisting of eight 20-bit words. Each word represented the compliment of the percentage of charge left on the integrating capacitor within the DDC112 chip. Data was split based on the state of the “convert” line. Convert A was associated with a low convert line and convert B was associated with a high convert line. This was necessary to remove differential biases between integrators.

Data was selected from a few minutes before lift-off as a relative dark reference. We sampled about 20 seconds worth of data and averaged each detector separately. These values were used as a baseline and subtracted from all flight data. The full scale brightness value was multiplied to the flight data matrix to convert the values to absolute brightness in watts per square centimeter per micron.

Care had to be taken to make sure that dark values averaged during convert A were subtracted from data measured during convert A and multiplied by saturation brightness values for detectors during convert A.

The second stage motor fin cant provided an intended roll rate of 4.5 Hz. A spectrogram performed on the Y axis magnetometer data showed a fairly constant 4.37 Hz until apogee (see figure 15). Just past apogee we see another spin frequency in the magnetometer data. Telemetry data shows second stage motor separation signal was sent coincident with payload reaching apogee. Down-leg flight was considered to be unstable so that data was not reduced.

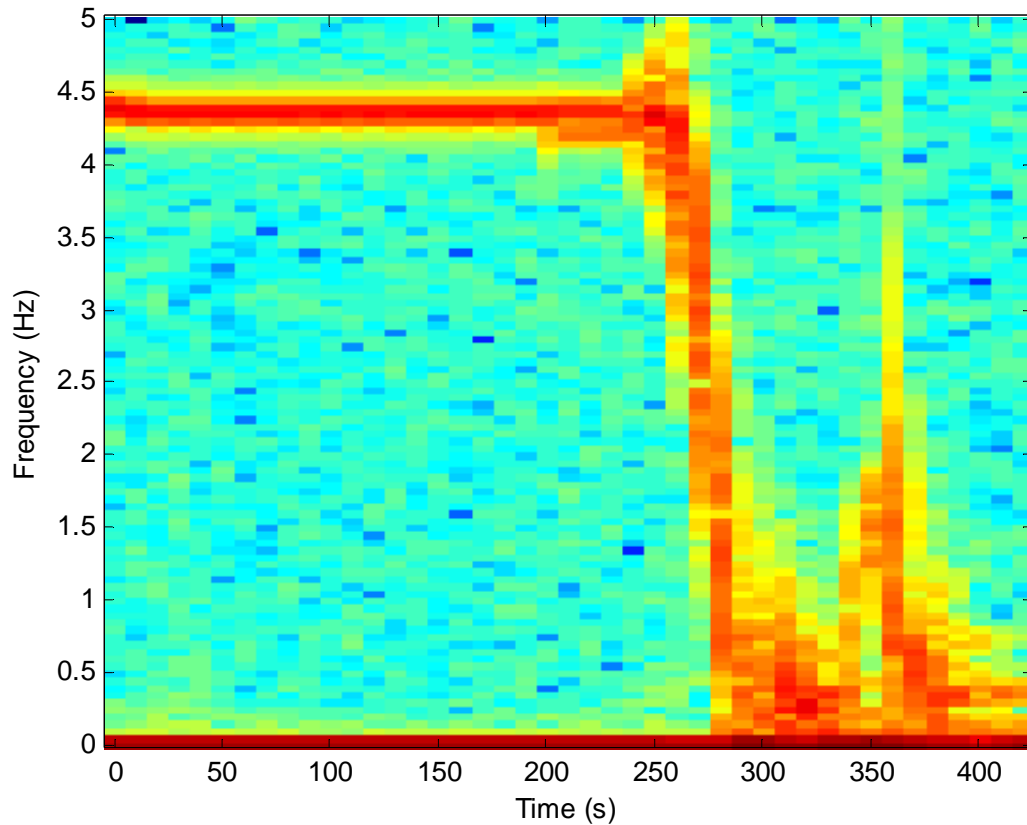


Figure 15. Spectrogram of Y axis magnetometer data showing a constant spin rate until apogee (around 200 seconds).

A fifth order Butterworth band-pass filter with a full-width half maximum of .01 Hz was applied to the flight data to remove fluctuations due to vehicle spin. The filter was applied through the data in both forward and reverse directions to help reduce any phase distortions introduced by a single filtering. This filter was chosen via an iterative method by applying the filter to the Y magnetometer data.

There appeared to be an approximate 10% drift in the data. This drift didn't appear to be related to any known influence on the vehicle. After eliminating vehicle

spin, power supply fluctuations, and any timed events through the payload we assumed that this was just a random electrical drift.

We discovered that the electrical drift affected the convert A data differently than the convert B data. As convert A data drifted slightly brighter the convert B data would drift slightly darker, and vice-versa (see figure 16). A set of running 9 point smoothed averages were laid over the flight data to show this was the case. We believe this may be due to minor fluctuations in the reference voltage changing the default charge on the capacitors inside the DDC112 chips. Since the convert line runs parallel to the reference voltage along most of the acquisition board there may be some capacitive coupling effects causing the convert A data to drift in an opposite direction as the convert B data.

Calculating the median between the two running averages showed a smooth data trend. The difference between the running averages and the median of the averages was subtracted from the actual flight data to eliminate this random electrical drift. After applying this correction a new running average was plotted to verify that the electrical drift was eliminated out of the flight data (see figure 17).

After de-interlacing the convert A and convert B data the vehicle spin became evident in the data again. A routine was written to allow fast processing of detector channels based on various filters. This routine would provide a series of three graphs of the Power Spectral Density of each detector in frequency space. The first graph showed the original flight data, the second graph was the chosen filter, and the third graph with the resulting data (see figure 18).

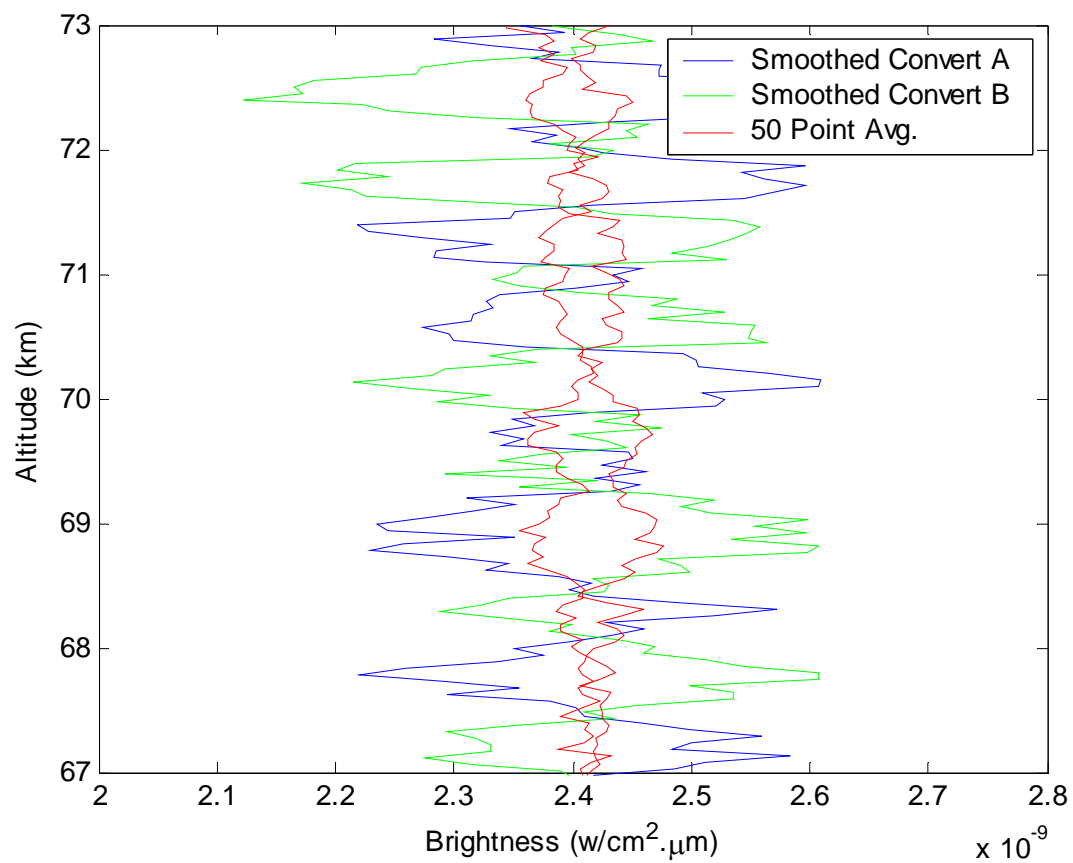


Figure 16. Drifting electrical noise evident in 1.364 μm center wavelength detector.

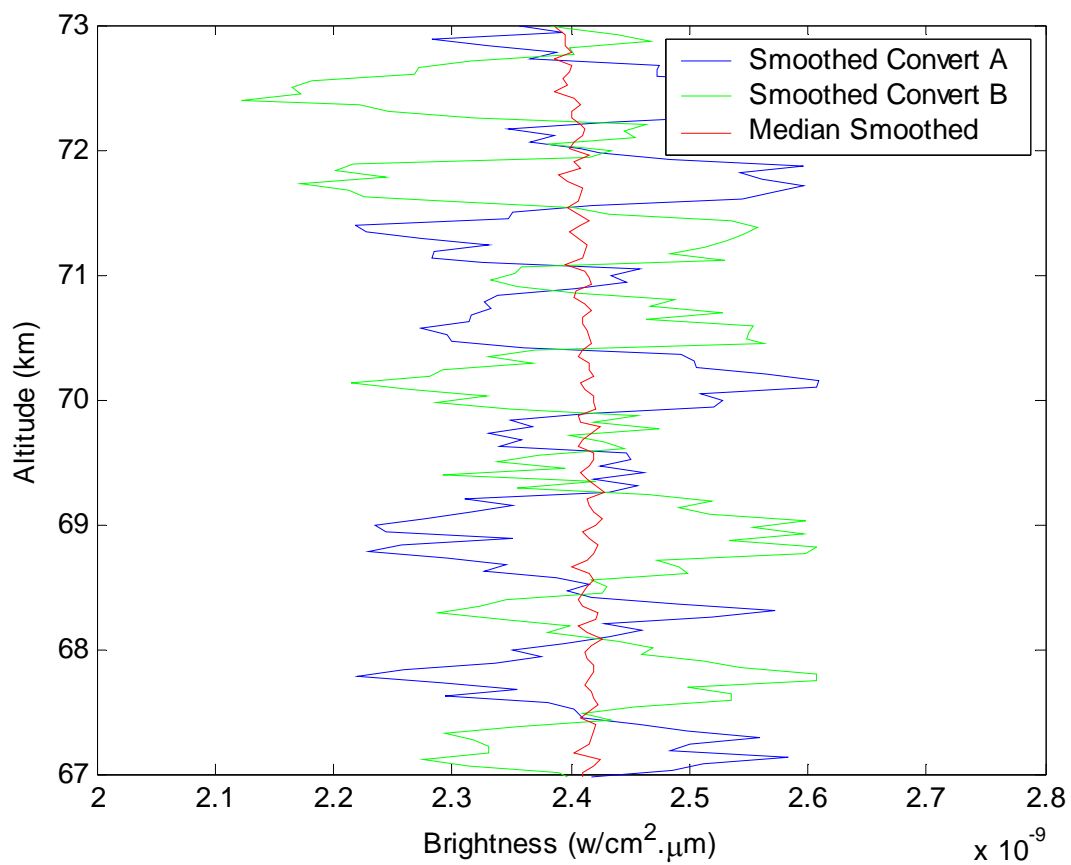


Figure 17. Vehicle spin evident in recombined optical data.

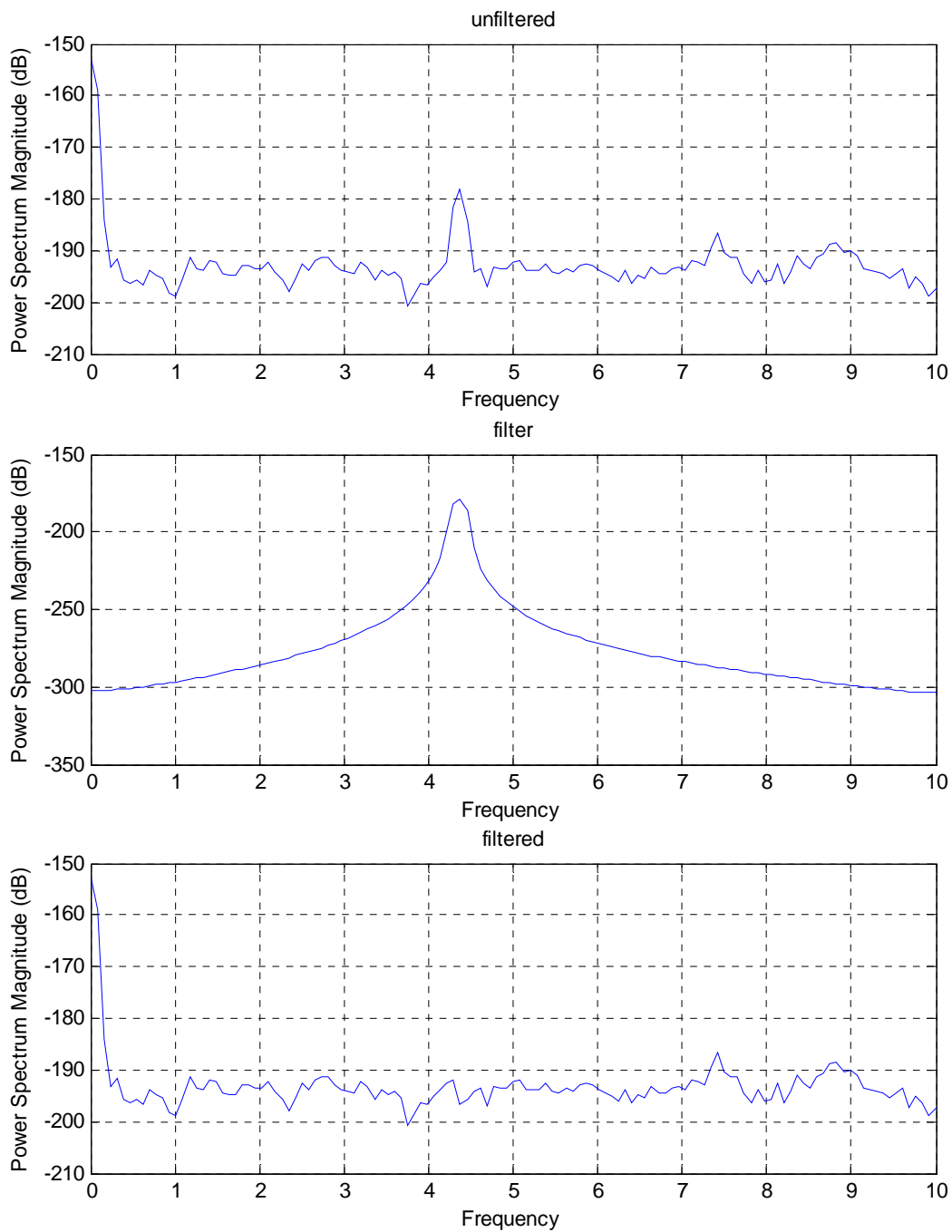


Figure 18. Effect of selected bandpass filter on overall flight data.

For each detector a unique filter was chosen based on how effective the filter was at removing the peak due to vehicle spin without altering the neighboring data. This time the Butterworth filter was applied with a full-width half maximum value between .005 Hz and .008 Hz, based on how the filter performed.

## V. Results

### A. Airglows

We recorded good optical data from the door deployment at 65 km until apogee. Optical data was transmitted real-time until loss of signal near touch-down, but loss of vehicle stability at apogee due to motor separation makes down-leg data complicated. Data collected during ascent is sorted into two bulk emission groups. The interval from 65 km to 90 km is dominated by the mesopause hydroxyl airglow region discussed in detail by A. B. Meinel [1950]. Above 90 km the signal level increases indicating the beginning of a vehicle induced emission (see figure 19) due to changes in atmospheric constituents.

The sharp feature at 96.5 km is due to a change in local atmospheric concentrations due to functions in the primary payload. A pneumatic valve is actuated six times during flight, venting approximately 700 ml (at STP) of helium gas about 6 inches behind the stagnation point. We believe that the sudden expansion of helium creates a cloud which inhibits atomic oxygen from reaching the vehicle skin. Signal processing tends to distort discontinuities in data such as this point, making this point appear artificially brighter than raw data indicates. Raw data shows the brightness drops to zero on most detectors during this event.

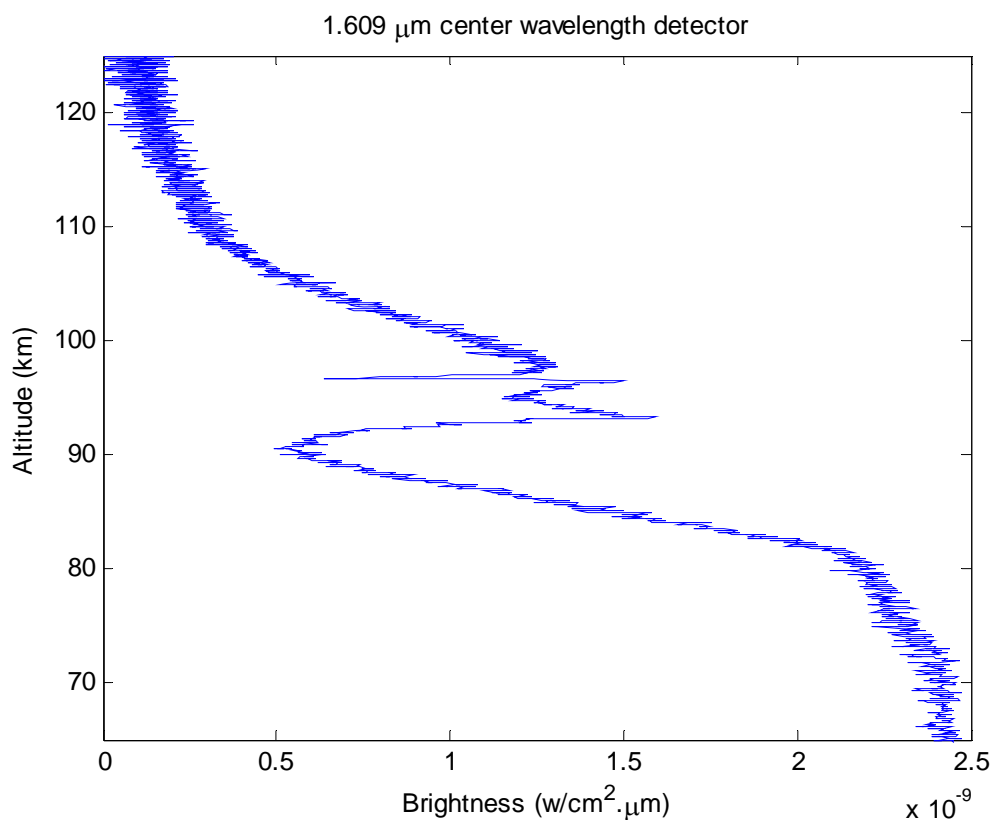


Figure 19. Data measured from 1.609 μm center wavelength detector.

Once the vibrations and shock from door deployment subside we immediately see the hydroxyl airglow in the mesopause region. Since the instrument is looking up, the measured light is the integral of all radiation above the vehicle. Taking the negative derivative of the data gives the change in brightness per altitude region. This change in brightness is the volume emission rate through this region. While we have continuous emission from 70 km up to past 89 km the bulk emissions are centered between 80 km and 90 km (see figure 20). This shows good agreement with previous measurements showing a peak OH nightglow density around 85 km [Llewellyn et al., 1978].

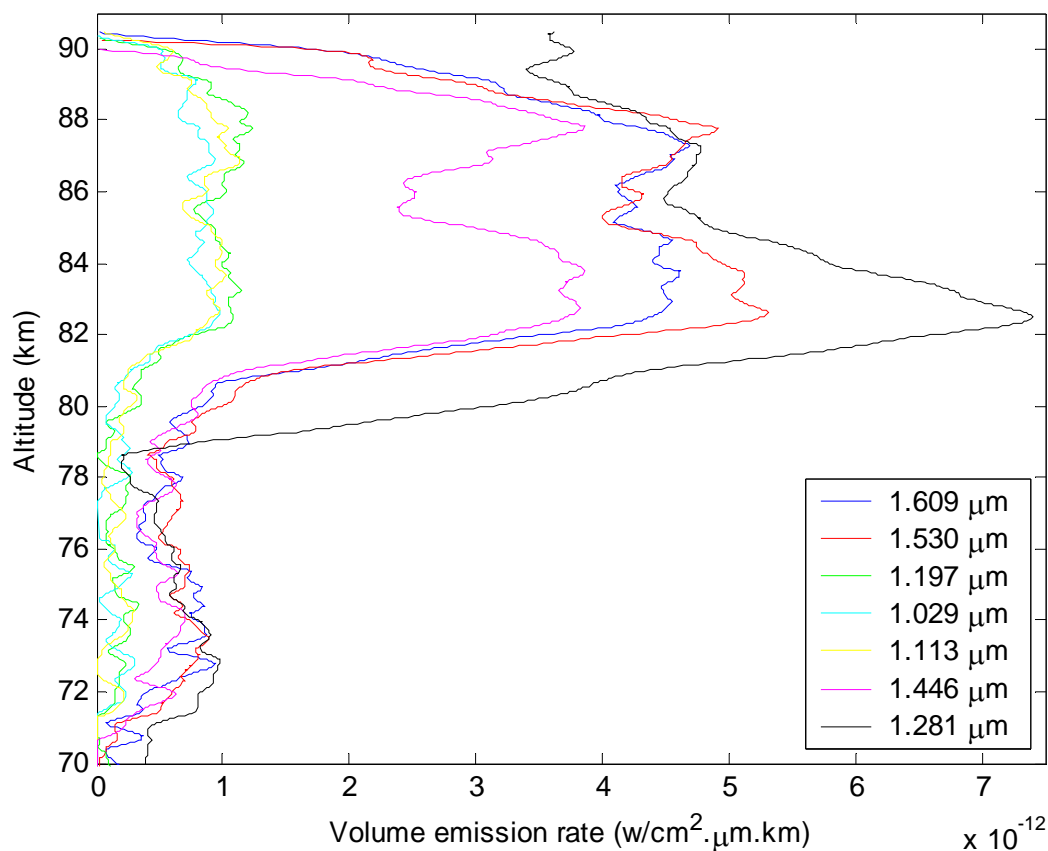


Figure 20. Volume emission rate of hydroxyl nightglow.

The double peak of OH emissions mentioned by Sivjee [1992] can be seen across all spectrograph channels. This double peak appears symmetric in emission rates on all detectors except for the measurements in the 1.281  $\mu\text{m}$  center wavelength detector. This detector measures a strong emission from the  $\text{O}_2$  ( $^1\Delta$ ) transition at 1.2675  $\mu\text{m}$  [López-Moreno et al., 1985]. The molecular oxygen density drops off rapidly throughout this region so the brightness doesn't appear symmetric across the peak pair. Evans et al. [1973] measured the 1.27  $\mu\text{m}$  band emissions along with 1.6  $\mu\text{m}$  and 1.8  $\mu\text{m}$ . They measured a pair of emission regions in their 1.27  $\mu\text{m}$  detector at 87 km and 96 km which

runs counter to that seen during this flight or that seen by Murtagh et al. or López-Moreno et al. It is interesting to note that Evans et al. measured a second volume emission region around 100 km. They postulated that another OH production mechanism or, “a background galactic component or a subvisual auroral glow,” may be responsible [Evans et al. 1973].

The apparent sharp drop in the volume emission rate of OH at 90 km is artificial (see figure 20). At this altitude we begin to see a rapid increase in signal level unrelated to the OH airglow (see figure 21). While the Murtagh et al. [1997] paper shows a small increase in brightness at this altitude the vehicle glow in both papers appears to start increasing closer to 93 km. This increased emission at 90 km is the beginning of the vehicle induced emission.

Murtagh et al. [1997] successfully fitted the vehicle glow to the square of the vehicle velocity times the square of the atomic oxygen density measured simultaneously during flight (see figure 29). Using the MSIS-E-90 Atmospheric Model to generate a synthetic atomic oxygen density profile for White Sands Missile Range (on July 15, 2003 at 1am local time at latitude 32.45N longitude 106.44W) we were able to find only moderate agreement with the model proposed by Murtagh et al. [1997]. Although the decrease in signal from 98 km until apogee corresponds well with the atomic oxygen density (see figure 21), lower altitudes fail to match well, indicating either a local deviation from the MSIS 90 fit or additional unknown mechanisms.

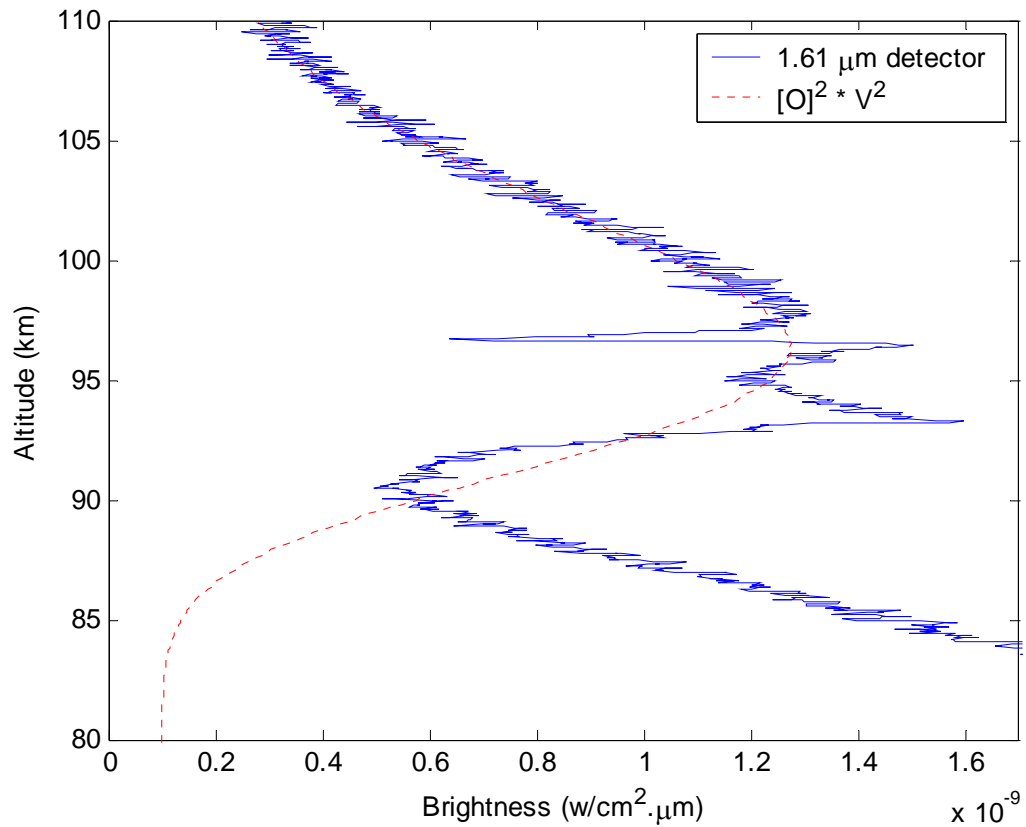
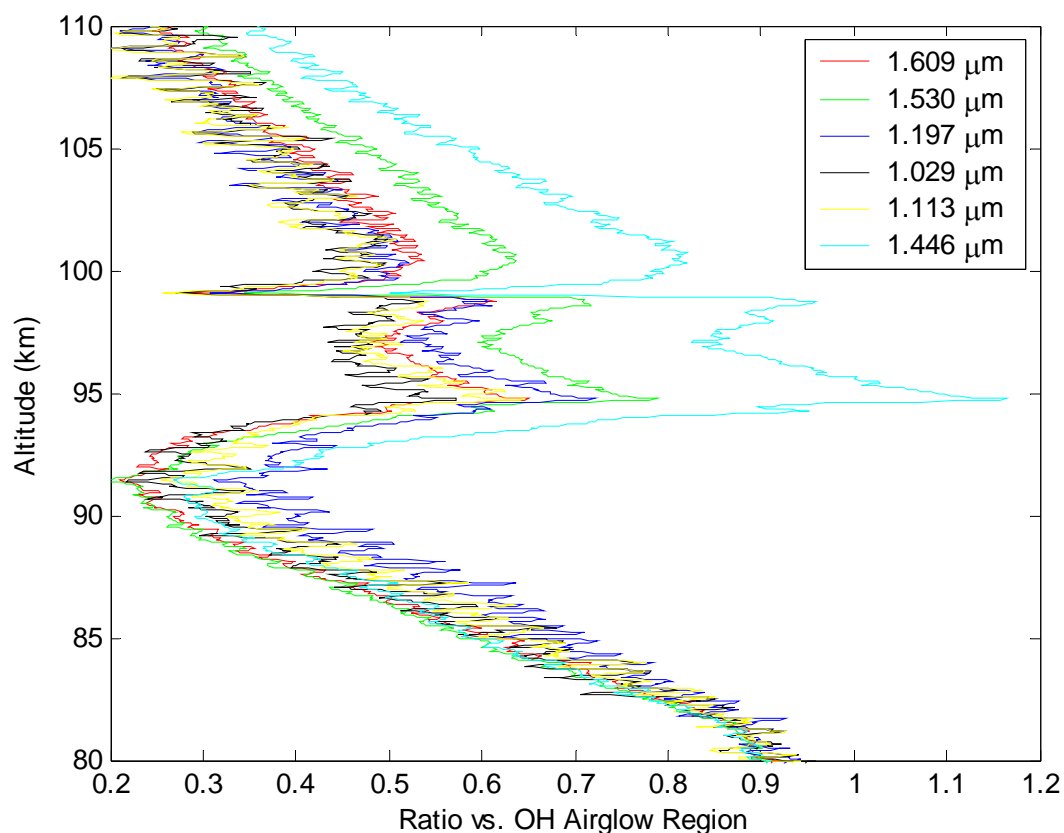


Figure 21. Vehicle induced glow compared to atomic oxygen model.

If the vehicle induced glow is similar to the hydroxyl airglow we would expect the relative intensities of various wavelengths seen in the hydroxyl airglow to maintain the same proportions within the vehicle induced glow region. This can be analyzed visually by normalizing each detector to the integrated overhead airglow brightness measured from 65 km. As a general trend the vehicle induced emission is lower in brightness than the integrated airglow region (see figure 22).



**Figure 22.** Vehicle glow from six detectors normalized to the vertically integrated hydroxyl emission brightness.

Two particular detectors, centered at 1.45  $\mu\text{m}$  and 1.53  $\mu\text{m}$ , detect enhanced emission above the trend from the airglow region. Whatever mechanism is creating the vehicle induced emission enhances radiation around 1.45  $\mu\text{m}$  and 1.53  $\mu\text{m}$ . Using the synthetic spectrum generator written by Dr. Patrick Espy [*private communication*] coupled with calculated Meinel Band intensities in the nighttime airglow [Llewellyn, 1978] we can generate the relative emission intensities of the various OH emission bands (see figure 23). Despite the wide bandwidths used in our spectrograph we can still determine some useful trends in the data.

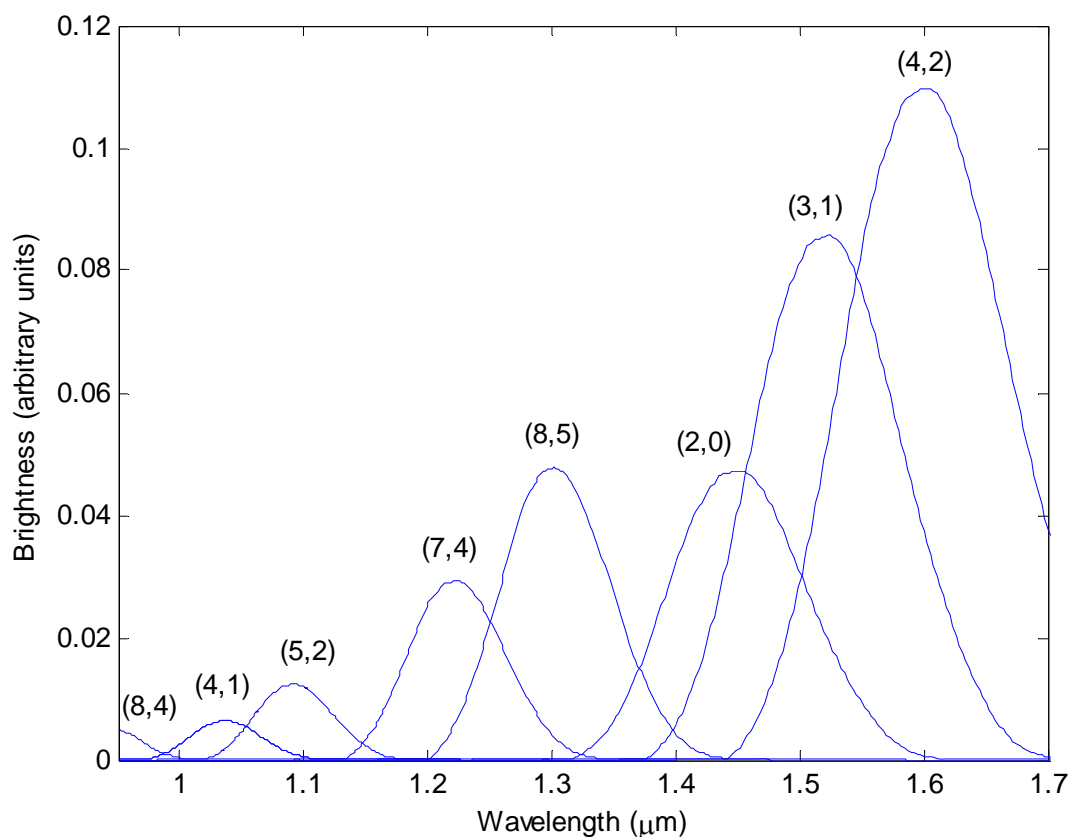


Figure 23. Relative integrated airglow intensities of various hydroxyl transitions in the near-infrared with a full-width half maximum  $0.05 \mu\text{m}$  triangular bandpass.

Both  $1.45 \mu\text{m}$  and  $1.53 \mu\text{m}$  center wavelength detectors measure radiation primarily from the OH (2,0) and OH (3,1) transitions. The  $1.53 \mu\text{m}$  center wavelength detector picks up a significant contribution from the OH (4,2) transition as well. All of these transitions are from OH  $v' < 4$  with transitions of  $\Delta v=2$ . Emission at  $1.61 \mu\text{m}$ , consisting primarily of OH (4,2) emissions with a small contribution from OH (3,1), shows negligible preferential emission through the vehicle induced emission region. This leaves the OH (2,0) transition as the prime candidate for the enhanced emission.

Figure 24 shows the relative contribution from each OH transition for each detector. If the OH (2,0) transition is the only enhancement in the vehicle induced glow we would expect to see nearly three times the enhancement in the 1.446  $\mu\text{m}$  center wavelength detector as we see in the 1.530  $\mu\text{m}$  center wavelength detector. Taking a closer look at the vehicle induced glow above 100 km shows the ratio of enhanced radiation matches what we would expect from an enhancement solely from OH (2,0) emissions (see figure 25).

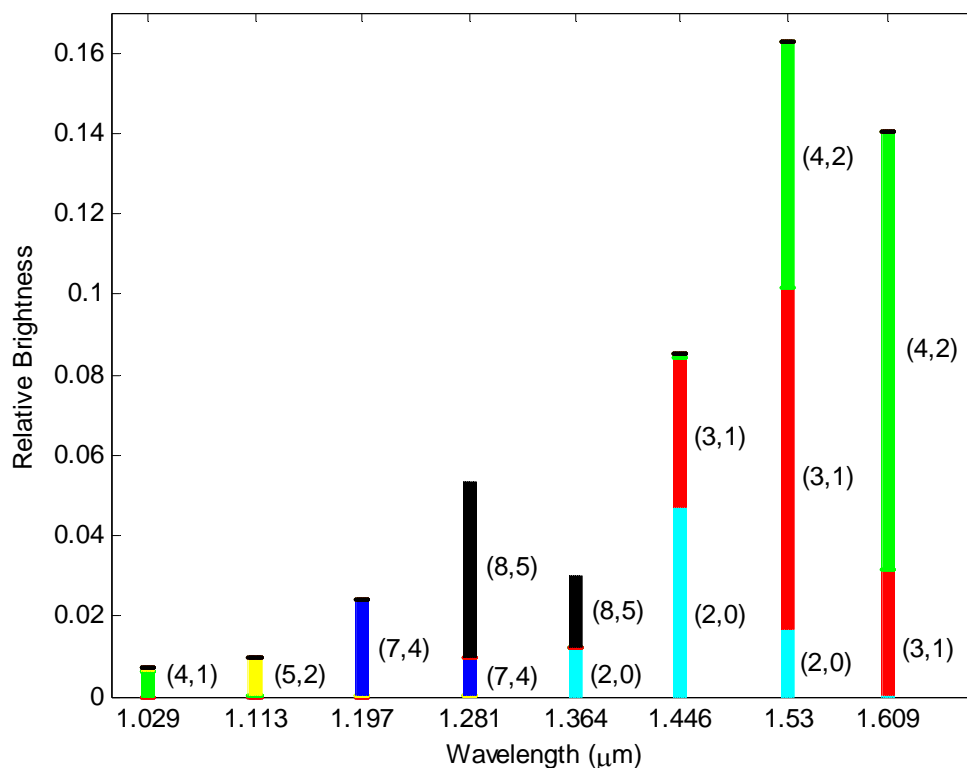


Figure 24. Relative contributions to detector input from various OH transitions.

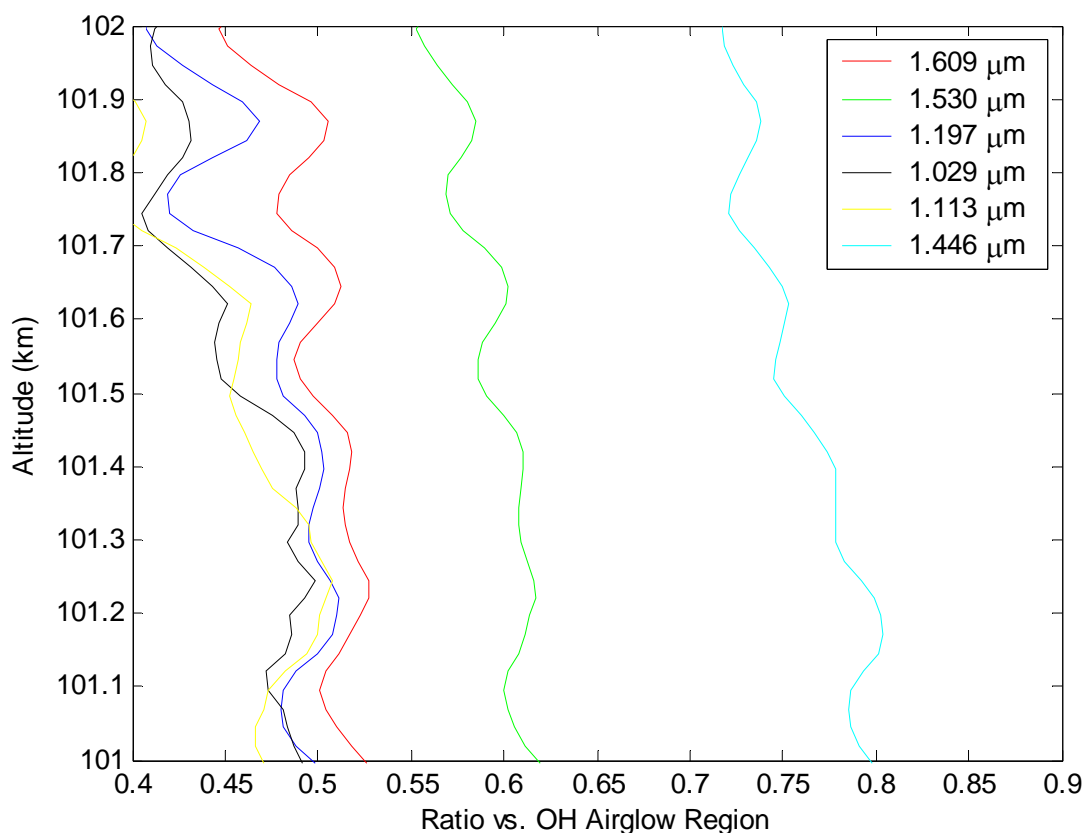


Figure 25. Ratio of vehicle induced glow at 101 km to integrated airglow seen from lower altitudes.

Another detector which measures radiation due to the OH (2,0) transition is centered at 1.36  $\mu\text{m}$ . The data from this detector shows almost no change in brightness between 70km and 90km. This gives some indication that the dominant background radiation in this region is not from OH transitions but from some other glow emanating from a region above the hydroxyl airglow region. The vehicle induced radiation from this detector is still significant (see appendix A) reinforcing the theory that the OH (2,0) emissions are enhanced during this region.

The considerable contribution from the  $O_2 (^1\Delta)$  transition into the 1.281  $\mu\text{m}$  center wavelength detector inhibits critical analysis of the measured radiation. The lack of significant enhancement in the vehicle induced region is expected due to the lack of any contribution from the OH (2,0) transition in this channel.

Battaner and López-Moreno [1979] and Llewellyn et al. [1978] showed the airglow intensities are brighter for OH transitions of  $\Delta v=2$  than  $\Delta v=3$  especially for  $v' < 6$ . This appears to become more predominant in the vehicle induced glows as the ratio of  $\Delta v=2$  emissions to  $\Delta v=3$  emissions increases.

In general we show good agreement with data from López-Moreno et al. [1985]. The 1.28  $\mu\text{m}$  center wavelength detector from this flight showed a linear decrease in brightness up to around 100 km and maintains near zero brightness after that until apogee similar to that shown in the López-Moreno et al. publication (see figures 26 and 27). The 1.53  $\mu\text{m}$  and 1.609  $\mu\text{m}$  center wavelength detectors show a similar trend also. In both flights the  $\sim 1.55 \mu\text{m}$  center wavelength detectors showed a stronger response to the vehicle induced airglow than the  $\sim 1.65 \mu\text{m}$  center wavelength detectors. The data from López-Moreno et al. showed an increase in emissions due to vehicle contamination around 92 km while this flight showed increases starting around 90 km.

López-Moreno et al. measure a fairly smooth curve over the vehicle induced glow region while our instrument measured a vehicle induced emission with two peaks between 95 km and 100 km. This lack of detail in the López-Moreno et al. graphs could be attributed to the slow sampling rate and smoothing performed during data reduction. Our double peak is not visible in the data published by Murtagh et al. however it is

clearly visible in the modeled fit to vehicle velocity and atomic oxygen density Murtagh et al. discovered.

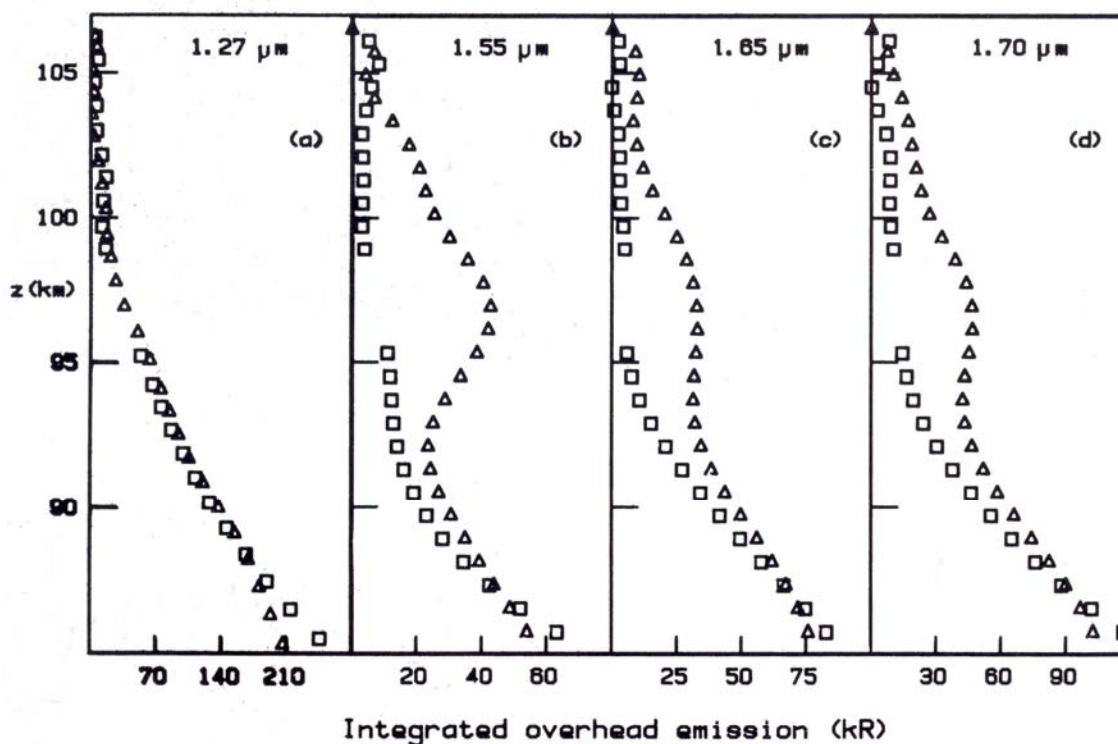


Figure 26. Integrated brightness from López-Moreno et al. publication [1985]. Triangles represent up-leg measurements, squares represent down-leg measurements.

This would reinforce the proposition by Murtagh et al. that, “it may be possible to infer the local structure in the [O] profile from the height variation of the ram glow.” [Murtagh, 1997]. Following this procedure we derived the atomic oxygen density through the vehicle induced emission region and compared it with the direct measurements of the atomic oxygen density taken by Murtagh et al. We show a weaker overall peak in atomic oxygen density yet good agreement on the dual peak structure as expected. We also see good agreement along the slopes, including the fine structure of

the atomic oxygen density at higher altitudes (see figure 28). The level of agreement between the two sets of data between 97 km and 103 km is certainly unexpected.

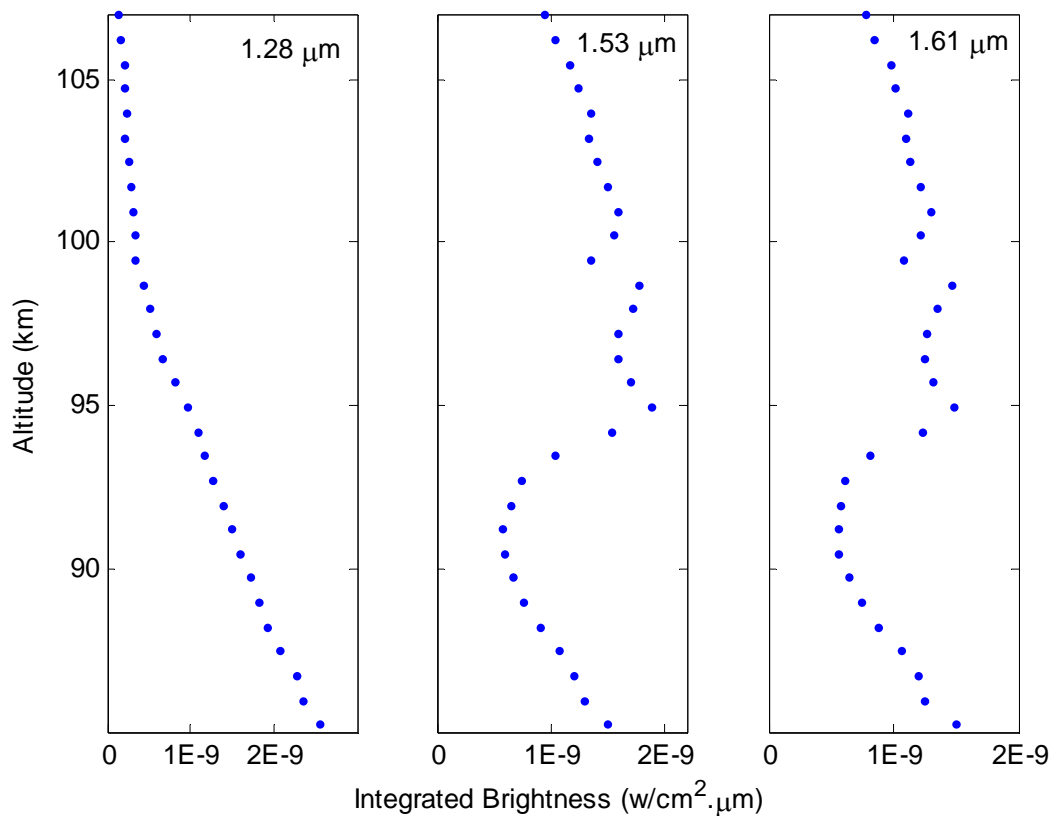


Figure 27. Integrated brightness of three detectors similar to those targeted by López-Moreno et al. [1985].

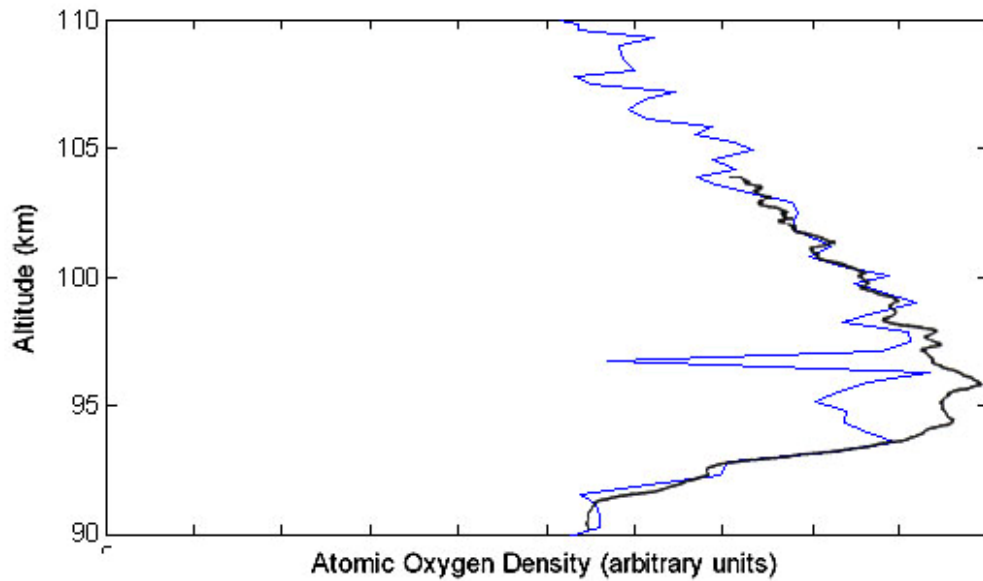


Figure 28. Derived atomic oxygen density compared with measurements from Murtagh et al. [1997]. The heavy line represents measurements taken by Murtagh et al. while the lighter line represents the derived density from this flight.

Murtagh et al. detected a vehicle induced emission much stronger than the hydroxyl airglow emission with their 1.53  $\mu\text{m}$  center wavelength detector (see figure 29). Dayglow intensities for  $\Delta v=2$  OH transitions are only one third that of their nightglow companion [Llewellyn et al., 1978]. This shows that the vehicle induced emission maintains a similar brightness from daytime to nighttime instead of following the intensity trends of the hydroxyl airglow region.

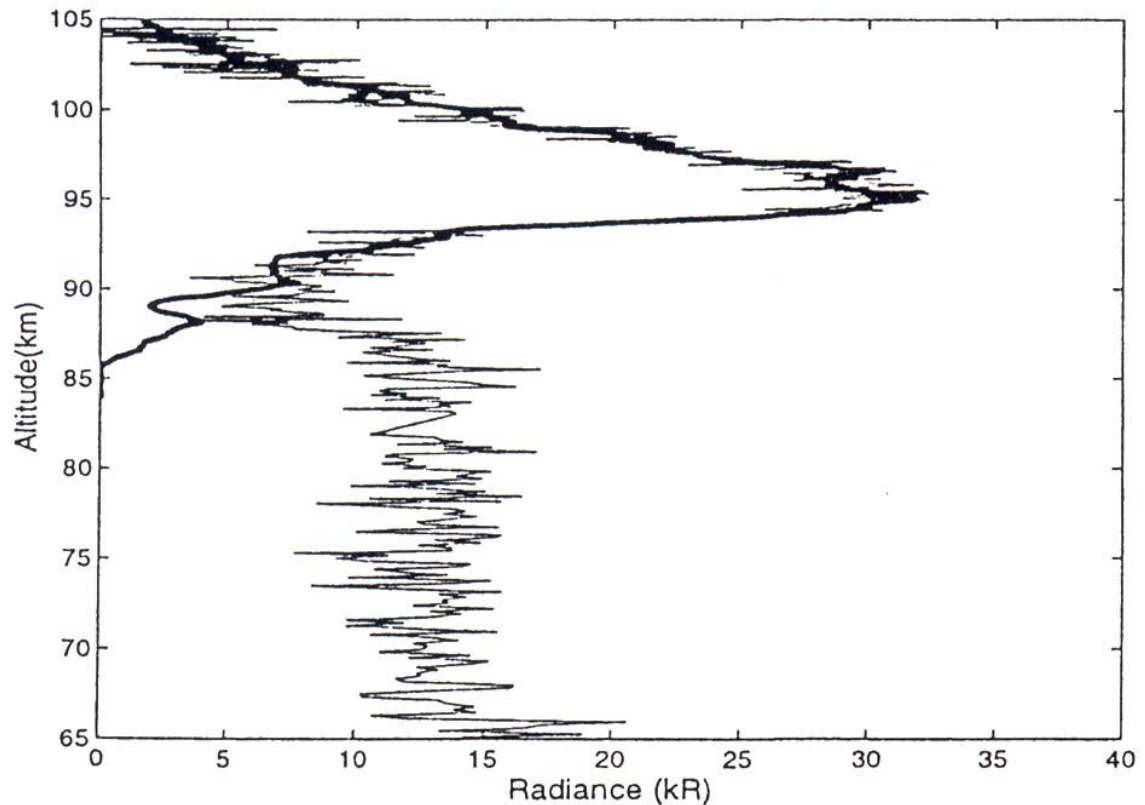


Figure 29. Data presented in the Murtagh et al. [1997] publication. Thin line shows measured brightness from  $1.53 \mu\text{m}$  after removal of rayleigh scattering components. Heavy line shows modeled fit of vehicle velocity squared time the atomic oxygen density squared.

## B. Door Heating

In addition to the airglow and vehicle glow some additional data was collected. Prior to instrument door deployment the instrument data indicates an increase in signal level with time. At door deployment this additional signal disappears and is replaced by the expected integrated hydroxyl glow.

We believe the instrument measured the optical radiation due to the aerodynamic heating of the door. We see a general trend of door heating during acceleration and door cooling during deceleration (see figure 30). Since we haven't been able to find any published information on payload door heating we decided to investigate further.

The vehicle door covers the full field of view of the instrument and is made of Aluminum 6061-T6. The surface was milled with no polishing of the surface. Moderate oxidation was visible on the door. Emissivity is difficult to calculate and we had difficulty reproducing the result in the laboratory due to the excessive temperatures needed.

Actual temperature at lift-off was around 298 K.

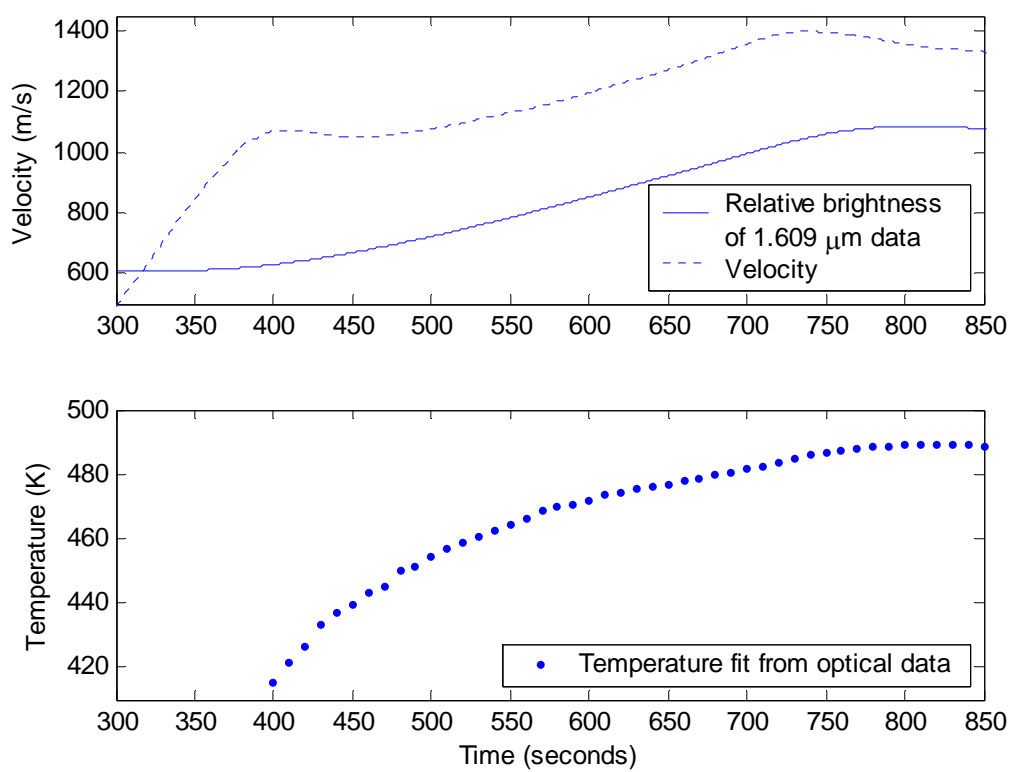


Figure 30. Heating of instrument door during ascent.

## VI. Conclusions

The data collected during this flight showed general agreement with previous measurements at similar altitudes and wavelengths [López-Moreno, 1985; Murtagh, 1997]. The vehicle induced glow is evident in the mesopause region just above the hydroxyl airglow region at various altitudes and seasons. This glow is almost undetectable at 1.281  $\mu\text{m}$  yet becomes a prominent feature around 1.5 – 1.6  $\mu\text{m}$ .

The vehicle induced emission can be modeled as a function of the product of vehicle velocity and atomic oxygen density, confirming a hypothesis by Murtagh et al. that the reverse is also possible. The sharp increase in atomic oxygen density around 93 km seen in this flight and by Murtagh et al. is not reflected in the MSIS-E-90 Atmospheric Model output.

Although the energy available due to atomic oxygen impact on this flight was twice that available for López-Moreno et al. (from 0.02 eV to 0.04 eV) the general distribution of excited OH does not seem to change. The mechanism generating the excited OH may be a thermoneutral reaction since any excess kinetic energy would be very small.

The vehicle induced emission spectrum follows closely with that of the hydroxyl airglow region, reinforcing the hypothesis that excited OH is a by-product of the vehicle contamination (and the source of the glow). While the brightness ratios between the two regions appears similar there is evidence to show that the OH (2.0) transition is preferential in the vehicle induced emission region. We believe this is a different mechanism than the  $\text{H} + \text{O}_3$  in the airglow region. It is still unknown if the upper vibrational states are populated during this OH generation. If the atomic oxygen is

recombining on the surface than there's a good chance that surface quenching could greatly reduce the upper vibrational populations.

It is interesting to note that the derived fine structure in the atomic oxygen density matches closely with that measured directly by Murtagh et al. [1997]. This could be a natural oscillation in the density or merely a byproduct of the smoothing function used to derive the density.

Further investigations into the mechanism of this glow would benefit from a tighter bandpass for higher wavelength resolution. The measurements taken from this flight could provide reasonably accurate brightness levels for future spectrometer designs investigating this phenomenon.

## REFERENCES

- Battaner, E. and J. J. López-Moreno, Time and Altitude Variations of the Vibrationally Excited States of Atmospheric Hydroxyl, *Planet. Space Sci*, Vol. 27, 1421, 1979.
- Clemensha, B. R., H. Takahashi, and Y. Sahai, Vehicle Glow Observed During a Rocket Sounding Experiment, *Planet. Space Sci.*, Vol. 35, 1367, 1987.
- Clemensha, B. R., H. Takahashi, and Y. Sahai, Contamination Glow Observed During Two Rocket Sounding Experiments, *Progress in Atmospheric Physics*, 109, 1988.
- Conway, R. R., and R. R. Meier, The Far Ultraviolet Vehicle Glow of the S3-4 Satellite, *Geophysical Research Letters*, Vol 14, 628, 1987.
- Erdman, Peter W., and Edward C. Zipf, In Situ Plume Radiance Measurements from the Bow Shock Ultraviolet 2 Rocket Flight, *Journal of Thermophysics and Heat Transfer*, Vol. 7, 704, 1993.
- Evans, W. F. J., E. J. Llewellyn, and A. Vallance Jones, Altitude Distributions of Hydroxyl Bands of the  $\Delta v=2$  Sequence in the Nightglow, *Can. J. Phys.*, 51, 1288, 1973.
- Fastie, William G., A Small Grating Monochromator, *Journal of the Optical Society of America*, Vol. 42, 641, 1952.
- Fastie, William G., Image Forming Properties of the Ebert Monochromator, *Journal of the Optical Society of America*, Vol. 42, 641, 1952.
- Llewellyn, E. J., B. H. Long, and B. H. Solheim, The Quenching of OH\* in the Atmosphere, *Planet. Space Sci*, Vol 26, 525, 1978.
- López-Moreno, J. J., R. Rodrigo, and S. Vidal, Radiative Contamination in Rocket-Borne Infrared Photometric Measurements, *Journal of Geophysical Research*, Vol. 90, 6617, 1985.
- Meinel, A. B., OH Emission Bands in the Spectrum of the Night Sky. I, *Astrophys. J.*, 111, 555, 1950.
- Mies, Frederick H., Calculated Vibrational Transition Probabilities of OH( $X^2\Pi$ ), *Journal of Molecular Spectroscopy*, Vol. 53, 130, 1974.
- MSIS-E-90 Atmosphere Model, June 2002, Retrieved February 9th, 2002, from [http://nssdc.gsfc.nasa.gov/space/model/models/msis\\_n.html](http://nssdc.gsfc.nasa.gov/space/model/models/msis_n.html).
- Murtagh, D. P., E. J. Llewellyn, and P. J. Espy, Infra-red rocket glow: A mechanistic analysis, *Geophysical Research Letters*, Vol. 24, 85, 1997.

Sivjee, G. G., Airglow Hydroxyl Emissions, Planet. Space Sci., Vol. 40, 235, 1992.

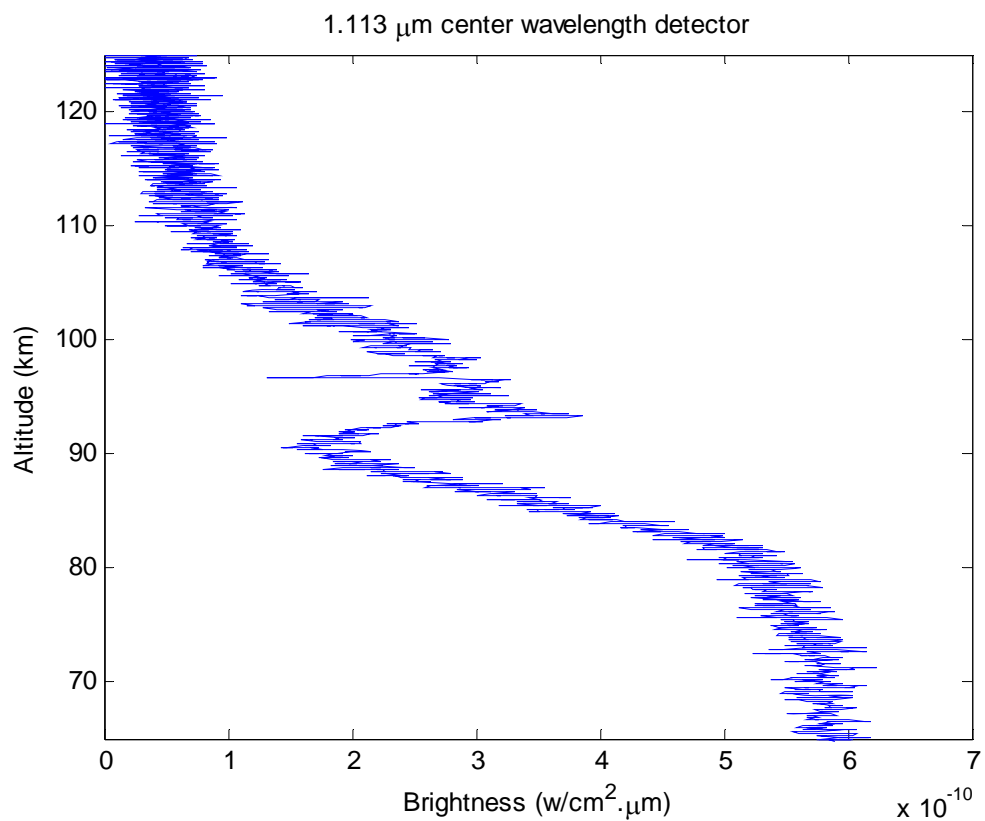
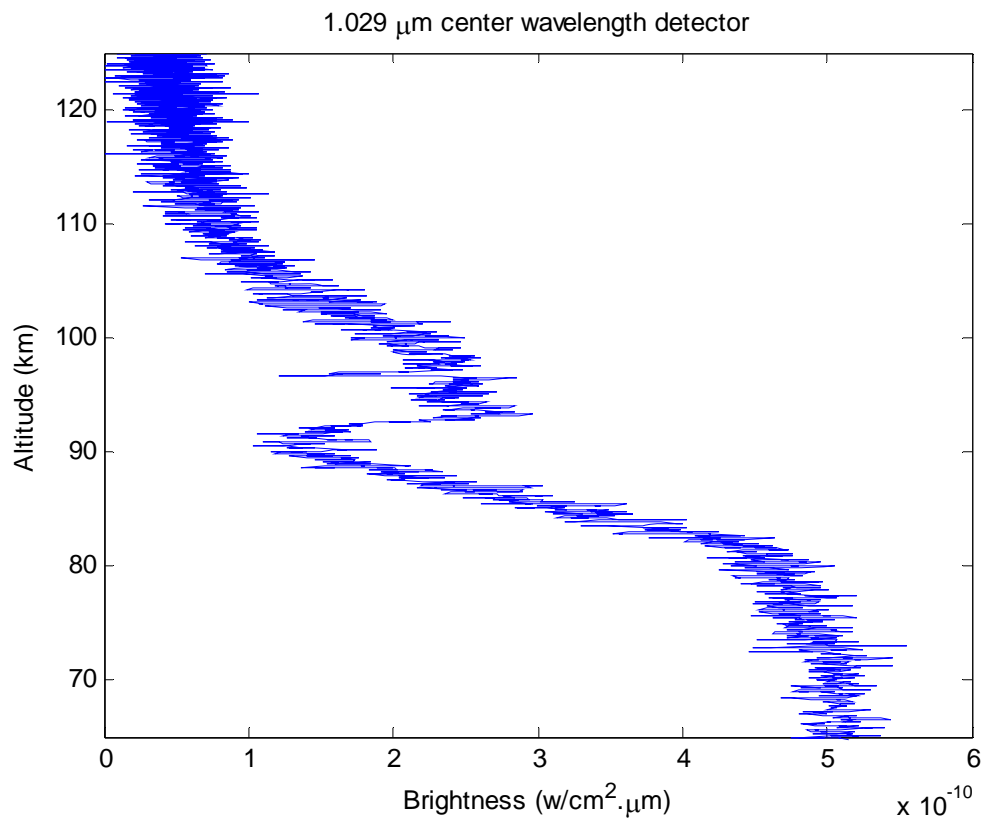
Swenson, G. R., S. B. Mende, and K. S. Clifton, Ram Vehicle Glow Spectrum; Implication of NO<sub>2</sub> Recombination Continuum, Geophysical Research Letters, Vol. 12, 97, 1984.

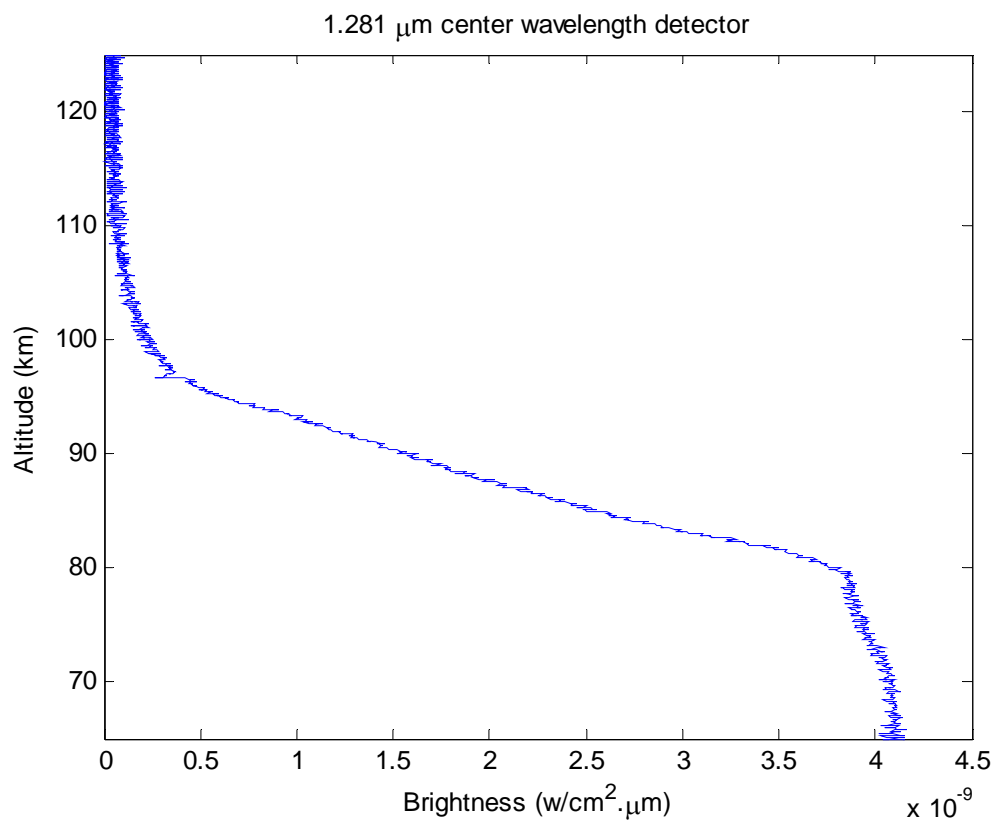
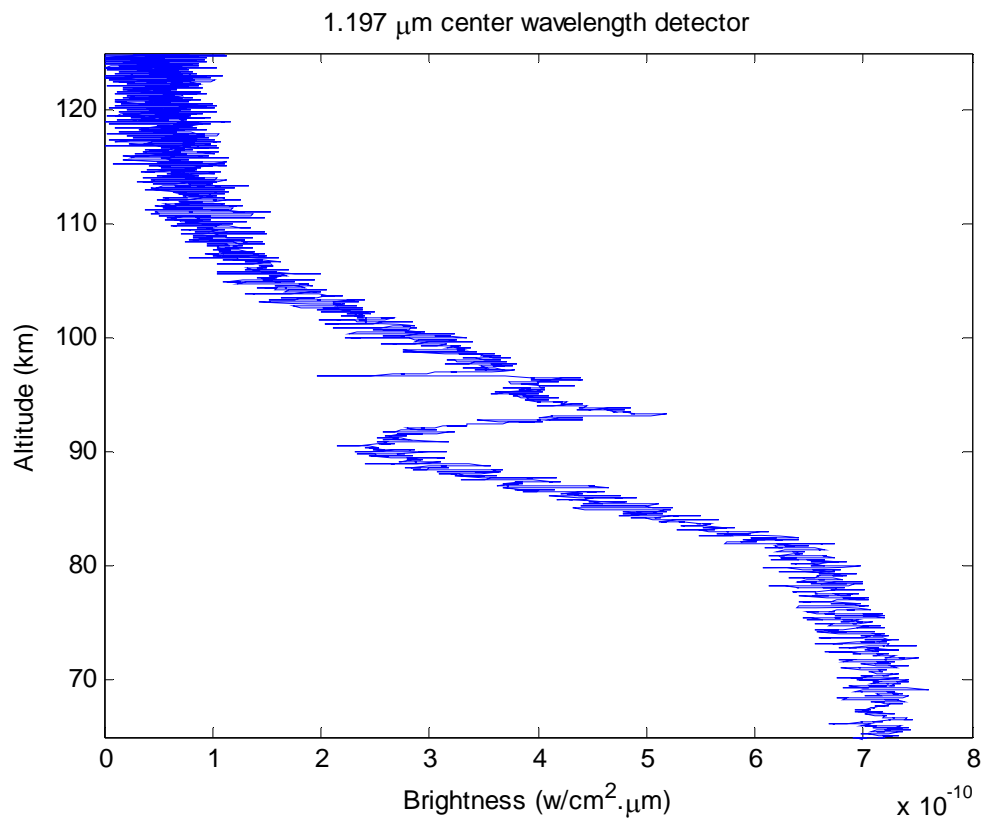
Yee, J-H., V. J. Abreu, and A. Dalgarno, The Atmosphere Explorer Optical Glow Near Perigee Altitudes, Geophysical Research Letters, Vol. 12, 651, 1985.

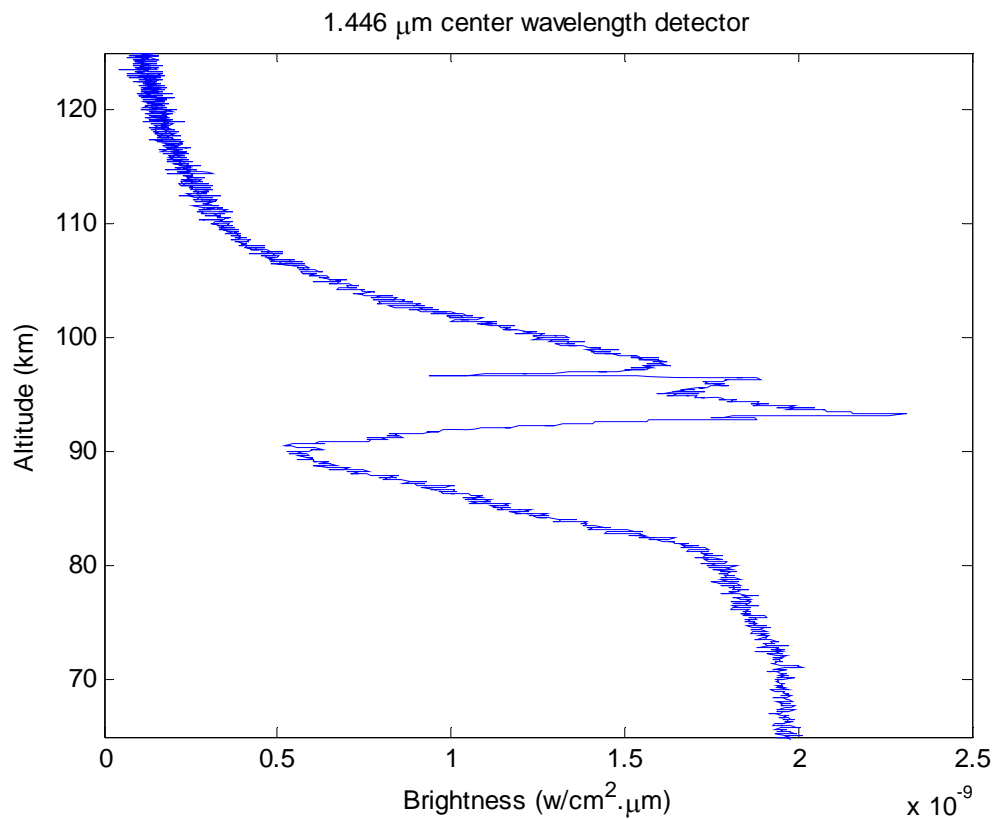
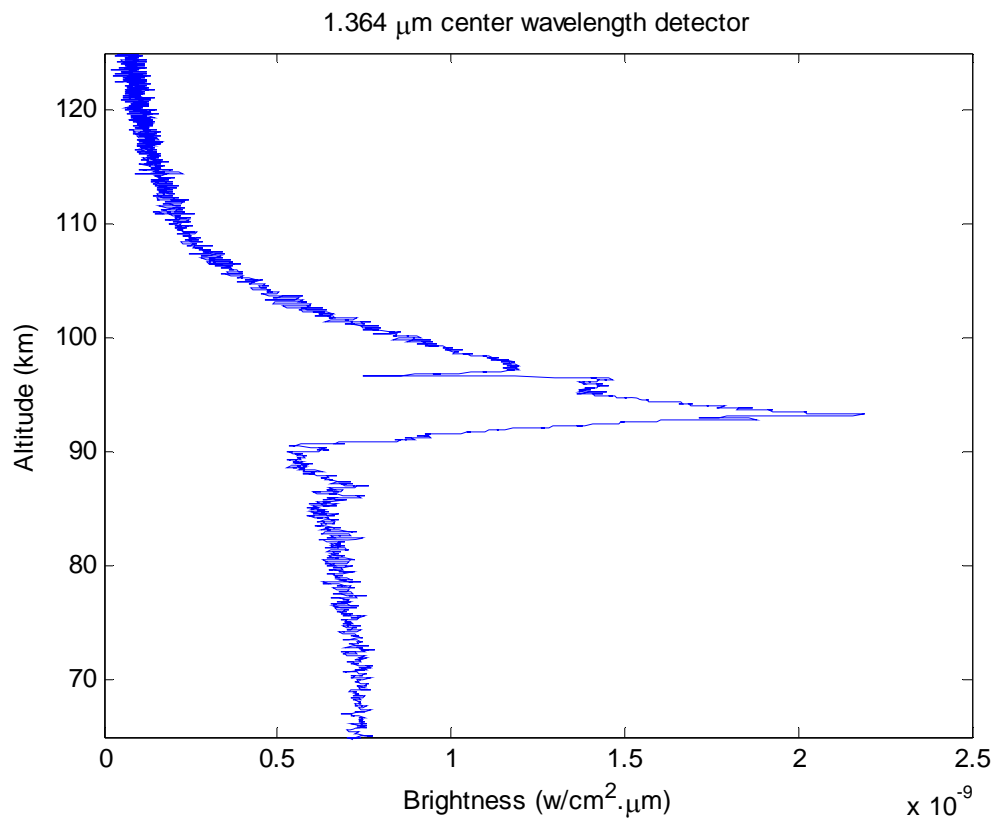
Yee, J-H, V. J. Abreu, Visible Glow Induced By Spacecraft-Environment Interaction, Geophysical Research Letters, Vol. 10, 126, 1983.

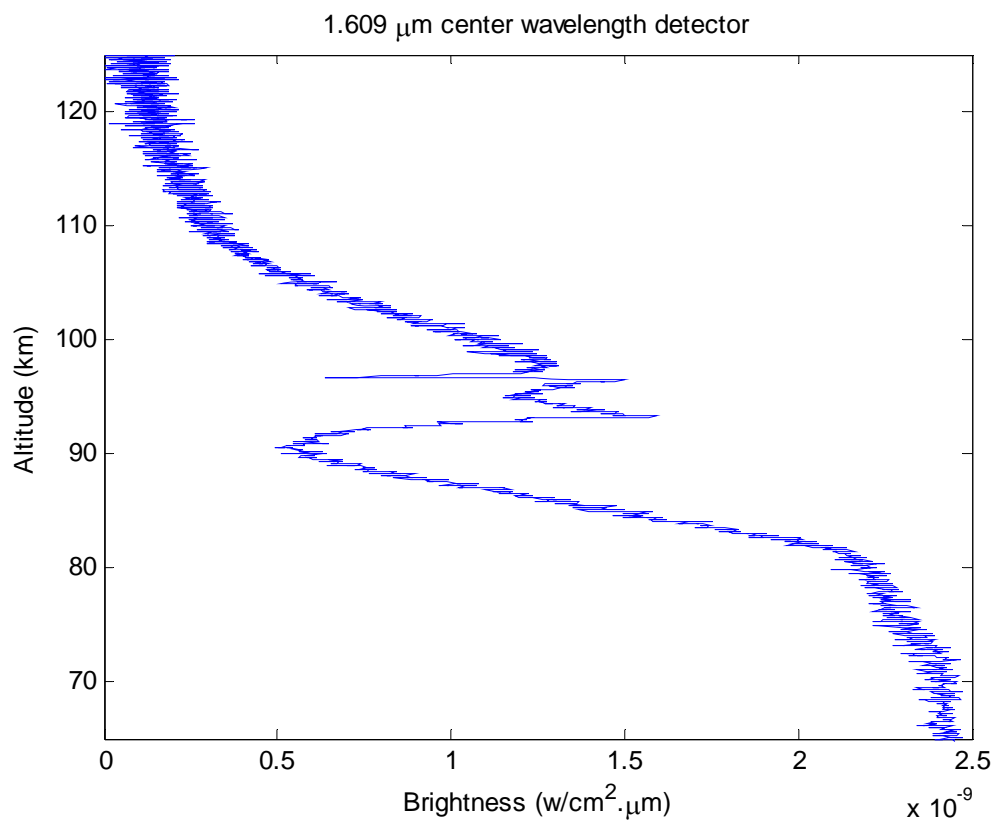
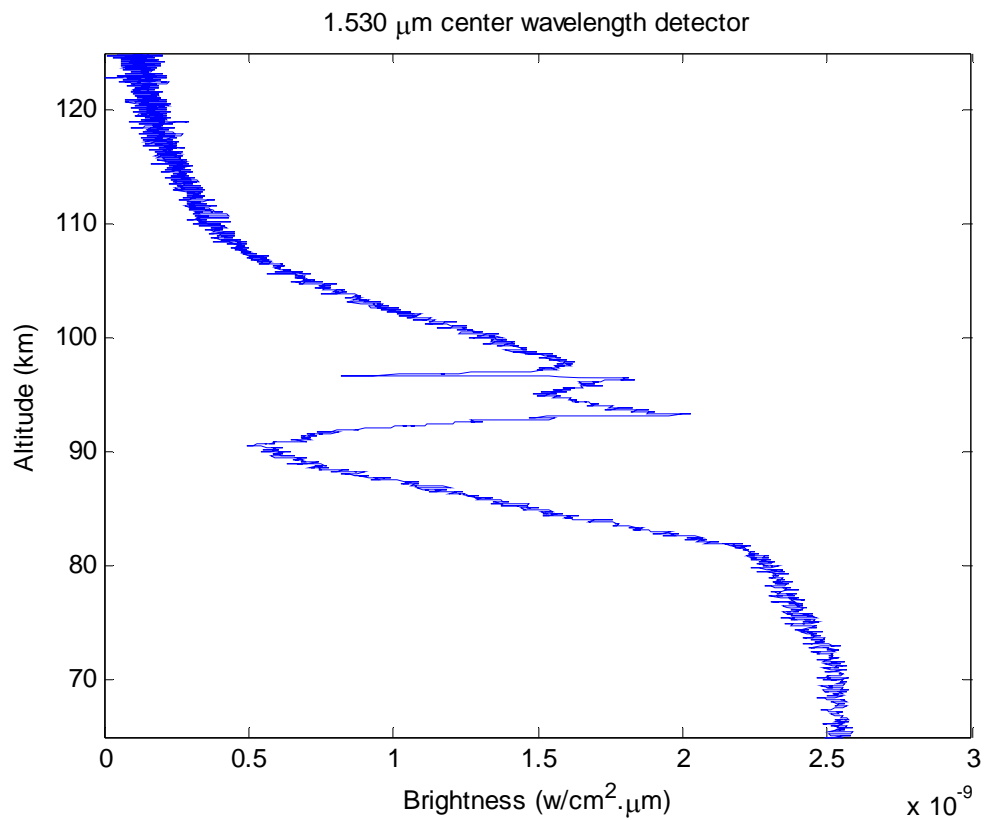
## **APPENDIX A**

**Flight data from all detectors from 65 km to 125 km**



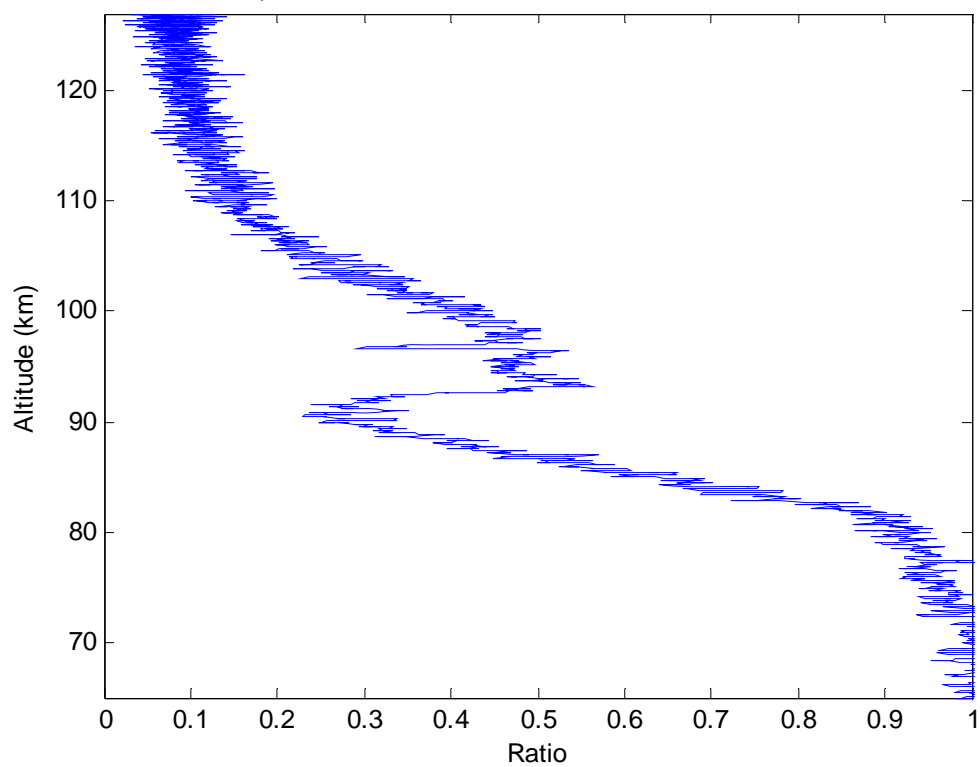
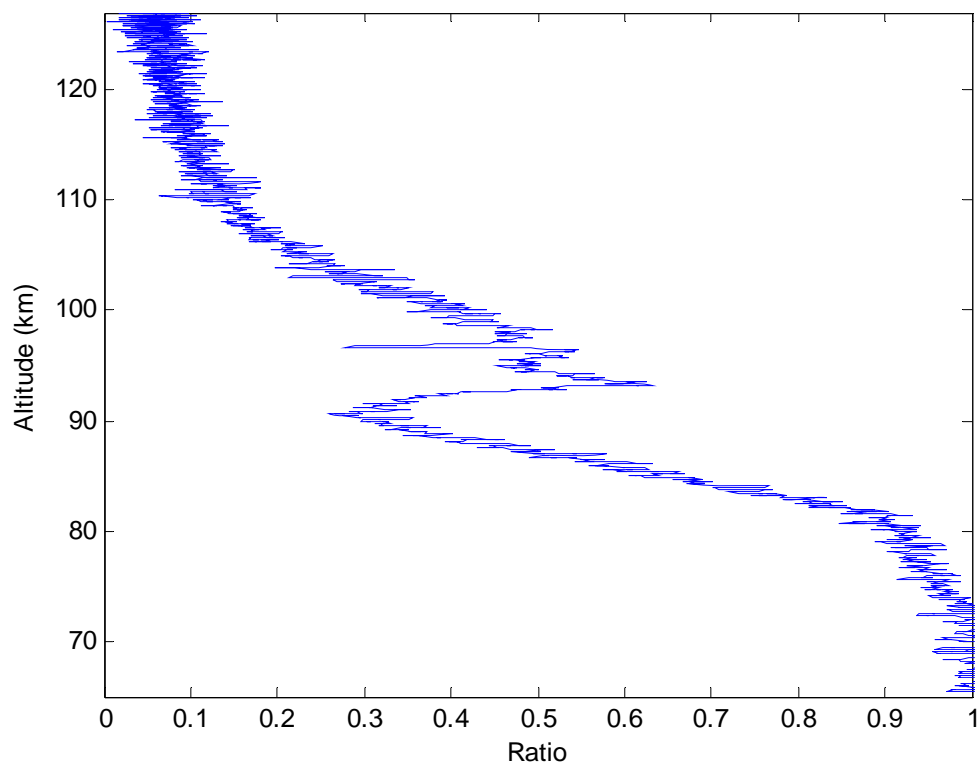


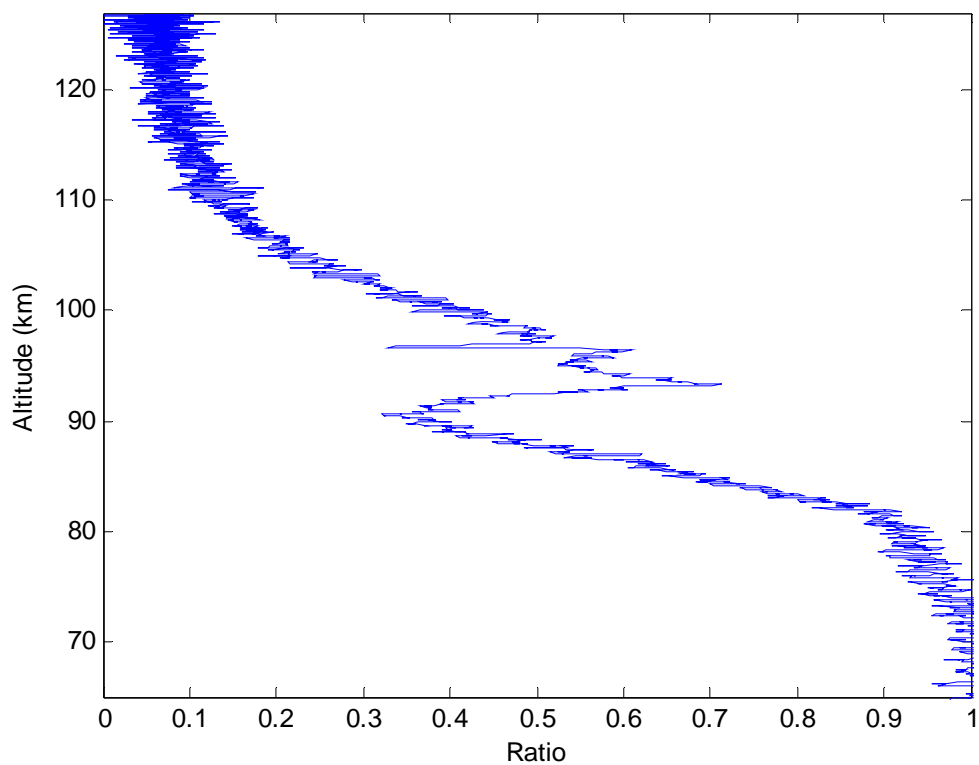
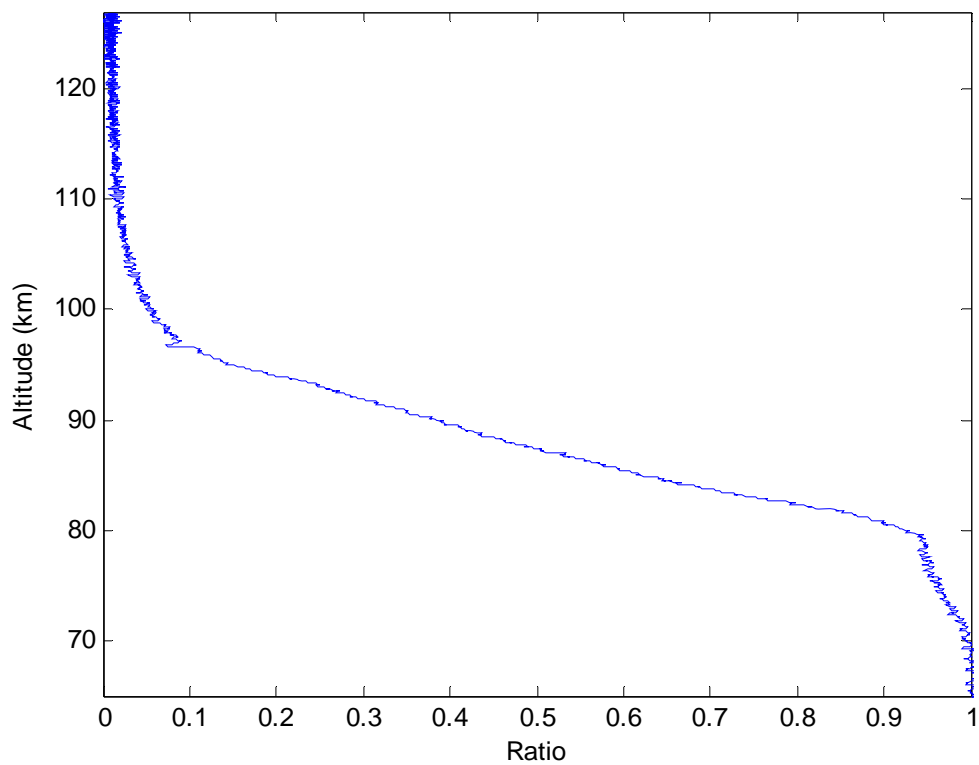


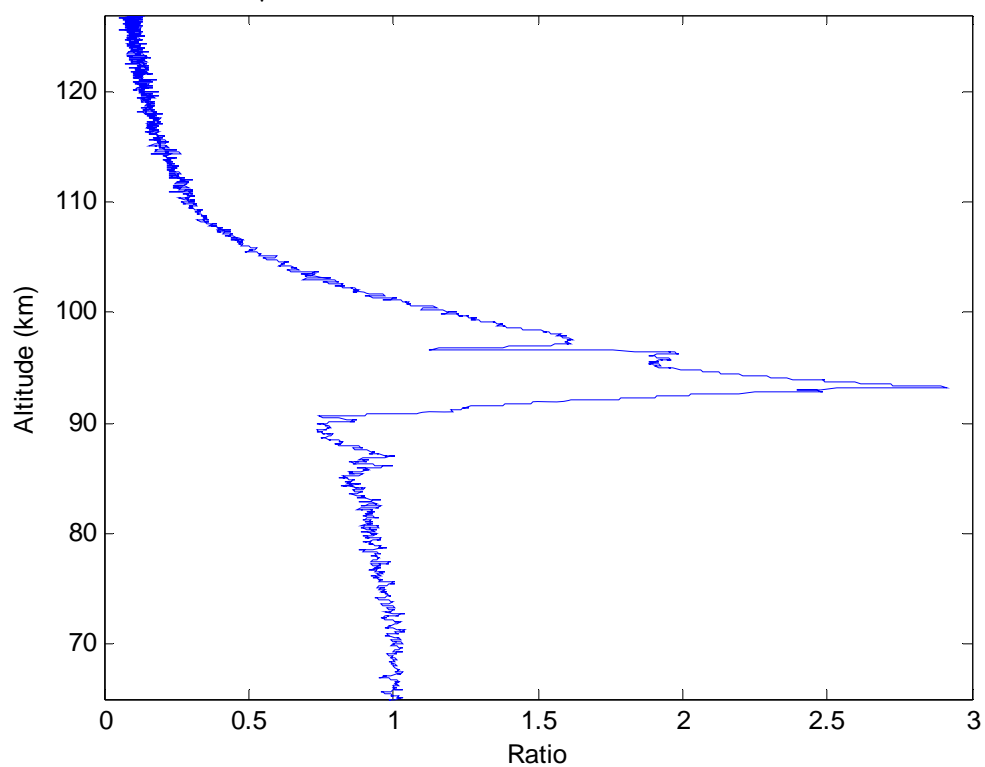
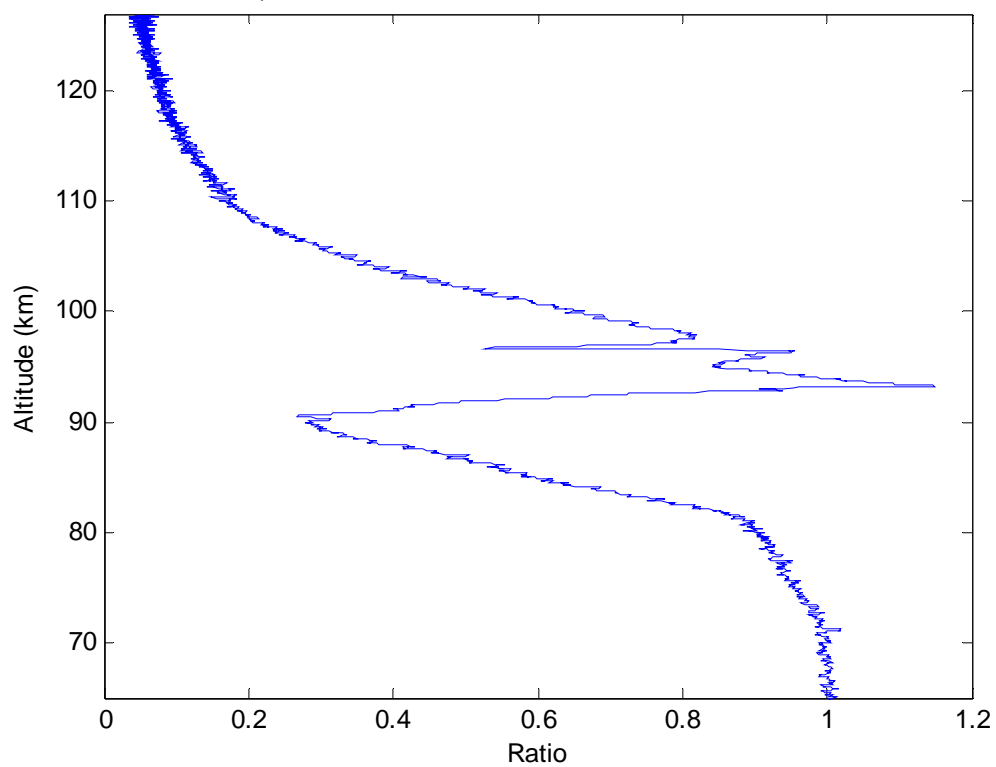


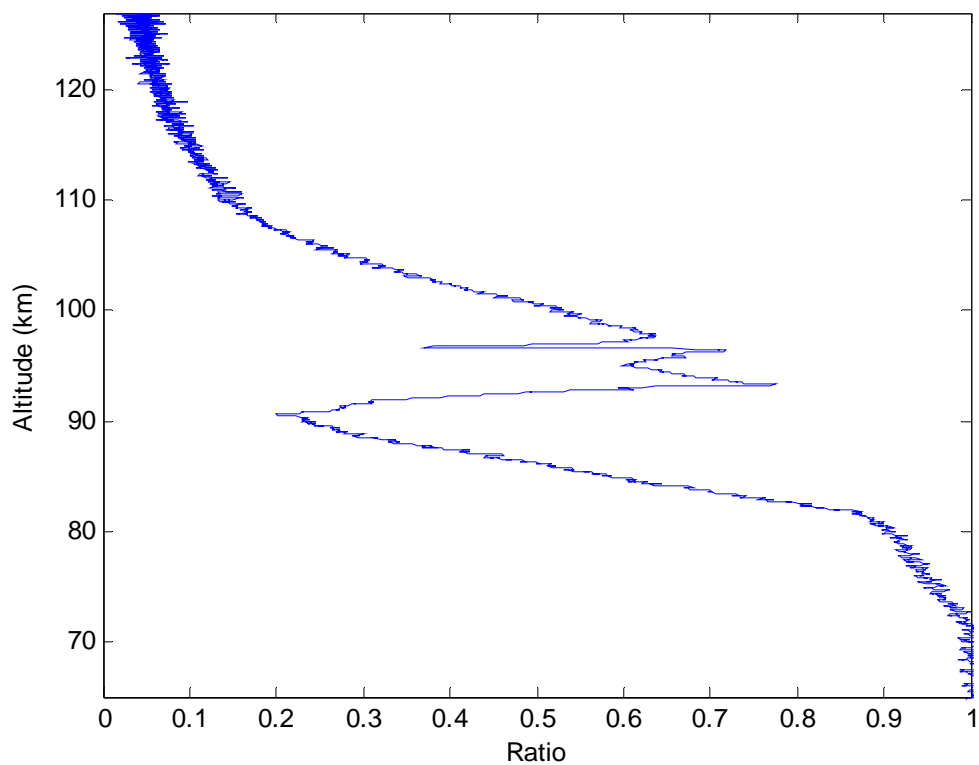
## **APPENDIX B**

**Flight data from 65 km to 125 km normalized  
to integrated OH glow seen above 65 km**

Data from 1.029  $\mu\text{m}$  center wavelength detector normalized to integrated OH glowData from 1.113  $\mu\text{m}$  center wavelength detector normalized to integrated OH glow

Data from 1.197  $\mu\text{m}$  center wavelength detector normalized to integrated OH glowData from 1.281  $\mu\text{m}$  center wavelength detector normalized to integrated OH glow

Data from 1.364  $\mu\text{m}$  center wavelength detector normalized to integrated OH glowData from 1.446  $\mu\text{m}$  center wavelength detector normalized to integrated OH glow

Data from 1.530  $\mu\text{m}$  center wavelength detector normalized to integrated OH glowData from 1.609  $\mu\text{m}$  center wavelength detector normalized to integrated OH glow